CrossMark

Alteration halos in the Tordillos sediment-hosted copper deposit of the Neuquén Basin, Argentina

María Josefina Pons [a,b,*], Marta Franchini [a,b], Adolfo Giusiano [c], Patricia Patrier [d], Daniel Beaufort [d], Agnes Impiccini [b], Ana Laura Rainoldi [a,e], Lawrence Meinert [f]

[a] Consejo Nacional de Investigaciones Científicas y Técnicas, Centro Patagónico de Estudios Metalogenéticos, Instituto de Investigación en Paleobiología y Geología Universidad Nacional de Río Negro, Avenida Roca 1242, 8332 Roca, Río Negro, Argentina
[b] Departamento de Geología y Petróleo, Facultad de Ingeniería, Universidad Nacional del Comahue, Buenos Aires 1400, 8300 Neuquén, Argentina
[c] Dirección Provincial de Hidrocarburos y Energía de la Provincia del Neuquén, Argentina
[d] Université de Poitiers, IC2MP, CNRS-UMR 7285, Hydrasa, Bâtiment B08, Rue Albert Turpin, F-86022 Poitiers Cedex, France
[e] Departamento de Geología, Universidad Nacional del Sur, San Juan 670, 8000 Bahía Blanca, Argentina
[f] EGRU, School of Earth and Environmental Sciences, James Cook University, Townsville, QLD, 4811, Australia

ARTICLE INFO

ABSTRACT

The Tordillos sediment-hosted Cu deposit is located in the north-central sector of the Huincul High structure, in the Neuquén Basin, Argentina. It is hosted in sedimentary rocks of the Huincul Formation, an Upper Cretaceous redbed sequence deposited in a fluvial environment. Field mapping, petrography, and chemical analysis of the authigenic clay, sulfate, carbonate, and sulfide minerals at Tordillos have identified systematic variation in alteration and paragenesis with time and with respect to the main feeder zones. The alteration associated with Cu mineralization provides evidence of a multistage infiltration of fluids spatially associated with paleo-hydrocarbon migration driven by Tertiary tectonism.

Early diagenesis formed hematite, kaolinite, and calcite1 that have been preserved in the reddish brown mudstones. Later influx of hydrocarbons and warm, reduced formation waters from deeper reservoir rocks is associated with dissolution of early cements and clasts and precipitation of new minerals. In the thickest paleochannels of the Huincul Formation, dissolution of early cements (hematite, kaolinite, calcite1 and barite1) and clasts locally increased the porosity of sandstones up to 24% and destroyed hematite that changed sandstones and conglomerates from red to yellowish-grey. Bitumen impregnations are abundant along with calcite2, 3, and 4, pyrite, minor montmorillonite, quartz overgrowth, and coarse barite2 crystals with primary organic fluid inclusions at the contact with hydrocarbon tubes. The MnO enrichment of calcite in stages 3 and 4 reflects their precipitation under reduced conditions. Grey and greenish-grey sandstones with montmorillonite, V-hematite, smectite-chlorite group minerals and pyrite, respectively are exposed between the reddish-brown mudstones and the yellowish-grey sandstones and conglomerates. The grey and greenish-grey horizons are representative of abrupt changes in Eh-pH conditions, between regional early oxidizing solutions responsible for the formation of early diagenetic redbeds and later infiltration of reducing fluids responsible for alteration of sedimentary rocks. Copper mineralization is located inside the altered sandstones and conglomerates zones, forming halos surrounding vertical tubes containing bitumen. These tubes are interpreted as the conduits through which migrated hydrocarbons, formation waters, and subsequent chloride and metal-rich fluids. In these places, pyrite, calcite, and barite cements of the altered rocks, have been dissolved and replaced by copper-rich sulfides and then by late supergene Cu minerals.

Interconnection among stacked permeable paleo-channels in the mid-section of the Huincul Formation facilitated the migration of several generations of fluids during early diagenesis, hydrocarbon up flow, and exhumation of the Neuquén Group, resulting in the development of alteration halos and Cu mineralization that can be used, both in outcrop and drill core, during exploration for sediment-hosted Cu mineralization.

© 2016 Elsevier B.V. All rights reserved.

* Corresponding author at: Consejo Nacional de Investigaciones Científicas y Técnicas, Centro Patagónico de Estudios Metalogenéticos, Instituto de Investigación en Paleobiología y Geología, Universidad Nacional de Río Negro, Avenida Roca 1242, 8332 Roca, Río Negro, Argentina.
E-mail addresses: jpons@unrn.edu.ar (M.J. Pons), mfranchini@speedy.com.ar (M. Franchini), agiusiano@neuquen.gov.ar (A. Giusiano), patricia.patrier@univ-poitiers.fr (P. Patrier), daniel.beaufort@univ-poitiers.fr (D. Beaufort), aimpicc@gmail.com (A. Impiccini), analaurarl@hotmail.com (A. Laura Rainoldi).

1. Introduction

The Tordillos deposit, one of 21 sediment-hosted Cu (V-U-Ag) deposits of the Neuquén Basin, western Argentina (Hitzman et al., 2005), is located in the Huincul High, near hydrocarbon fields and hosted in the Huincul Formation (Late Cenomanian-Early Turonian; Legarreta and Gulisano, 1989) of the Neuquén Group. Earlier publications about these deposits are descriptive and lack studies based on modern analytical techniques (Wichmann, 1972; Fernández Aguilar, 1945). Granero Hernández and Schmid (1956) identified for the first time bitumen impregnations in these rocks but did not associate the copper mineralization with hydrocarbons. Ramos (1975) interpreted the copper deposits as formed by alternations of dry and humid weather during Jurassic-Cretaceous sedimentation in the Neuquén Basin. In this model, meteoric water mobilized Cu, V, and U from the source rocks and precipitated these metals at contacts with vegetal organic matter. Lyons (1999) also interpreted a syngenetic-epigenetic origin for the Cu deposits. Recent studies (Giusiano et al., 2006, 2008; Pons et al., 2009; Pons et al., 2014; Rainoldi, 2015) proposed a new hypothesis that associates cupriferous mineralization with hydrocarbons and Cu-bearing brine migration along brittle structures of the Huincul High and Los Chihuidos High. This contribution presents detailed mineralogical and geochemical studies of the alteration zones in the Tordillos sediment-hosted copper deposit. These results document (1) the nature of fluids and the processes involved during early diagenesis, alteration, and mineralization of a Revett (Cox et al., 2003) or sandstone sub-type deposit (Zientek et al., 2015) and (2) alteration patterns that can be used as exploration guides for this deposit type in other parts of the Neuquén Basin.

2. Regional geologic setting

The Neuquén Basin is a complex retroarc foreland basin developed east of the Principal Cordillera, between 36°S and 41°S (Fig. 1A). The tectonic evolution of this basin began in the Late Triassic and Early Jurassic driven by extensional collapse of the Permian-Triassic orogenic belt, accommodated by a southwest-oriented extensional stress field (Vergani et al., 1995). Several episodes of structural inversion occurred, with the most significant in the Late Oxfordian-earliest Kimmeridgian, which marked the reorganization of extensional stress fields related to the fragmentation of southwestern Gondwana and the Atlantic opening (Vergani et al., 1995). This tectonic evolution is reflected in the 220 Ma stratigraphic record of basin subsidence with 7000 m of preserved Upper Triassic-Cenozoic basin fill and the development of source and reservoir hydrocarbon zones (Fig. 2).

The Huincul High, one of the most striking structures in the Neuquén Basin, is an intraplate deformation belt which extends 270 km with an E-W orientation (Figs. 1; 2A). The Huincul High consists of half-graben faults orthogonal to the Andes Cordillera formed in a right-lateral transpressive system (Mosquera and Ramos, 2006). This basement feature has been interpreted as a Paleozoic suture marking the collision between allochthonous Patagonia terrane to the south and the Gondwana continent to the north (Mosquera and Ramos, 2006).

Tectonic activity in the Huincul High began in the Late Triassic to Early Jurassic when the basement was affected by northwest-trending normal faults that bound a suite of discrete half-grabens (Vergani et al., 1995). The syn-rift fill (Pre-Cuyo Group) consists of coarse-grained continental sediments, volcanics, and volcaniclastic materials (Leanza et al., 2013). From the Early Jurassic onward, the evolution of the Neuquén Basin was characterized by regional subsidence interrupted by periodic inversion (Vergani et al., 1995). The Cuyo Group deposition (Pliensbachian-Bathonian) was largely confined to structural depocenters during an extensional regime driven by orogenic collapse (Uliana et al., 1989). Late Jurassic inversion is represented by the beginning of the Mendoza Group with the deposition of the basal fluvial

deposits of the Tordillo Formation and eolian deposits of Quebrada del Sapo Formation (Zavala et al., 2008). During the Late Jurassic and Early Cretaceous, a period of tectonic stability resulted in thermal subsidence with subsequent deposition of the marine shales of the Vaca Muerta Formation, the most important hydrocarbon source rocks (Legarreta et al., 2003) and unconventional reservoir rocks (Schmidt and Alonso, 2015).

The Early Cretaceous stage was characterized by a reduction in the areal extent of the Huincul High. The retreat took place along the eastern end of the Huincul High where Jurassic anticlines collapsed by extensional-transtensional faulting (Mosquera and Ramos, 2006). During Cenomanian times, renewed tectonic activity and inversion resulted in erosion and thinning of the Rayoso Group and accumulation of the continental deposits of the Neuquén Group (Fig. 2; Vergani et al., 1995), as a response to the compressional event related to the growth of the Andean fold and thrust belt to the west. Neuquén Group sedimentary rocks up to 1300 m thick lie unconformably on continental sedimentary rocks of the Rayoso Group (Aptian-Albian) and resulted from widespread fluvial, eolian and shallow lacustrine processes in the Neuquén basin (Cazau and Uliana, 1973; Legarreta and Gulisano, 1989; Condat et al., 1990; Sánchez et al., 2008; Garrido, 2011, and references therein). These rocks consist of three lithologic successions: the Río Limay Subgroup which includes the Candeleros, Huincul and Cerro Lisandro formations (De Ferrariis, 1968; Ramos, 1981), the Río Neuquén Subgroup which includes the Portezuelo and Plottier formations (Cazau and Uliana, 1973; Ramos, 1981) and the Río Colorado Subgroup which includes the Bajo de la Carpa and Anacleto formations (Cazau and Uliana, 1973; Ramos, 1981). The Neuquén Group is covered by marine sedimentary rocks of the Malargüe Group (Lower Campanian-, Danian, Parras et al., 2004 and references therein) (Fig. 2A).

During the Tertiary and especially the Miocene stage, deformation included additional tectonic inversion, and folding of Neuquén Group strata. Finally, during the Pliocene the Huincul High collapsed due to development of extensional structures (Mosquera and Ramos, 2006). Some faults close to the main fault originated in shallower levels and cross-cut the base of the Neuquén Group (Upper Cretaceous; Schiuma et al., 2002; Fig. 2A).

3. Methodology

Outcrops of mineralized, altered, and unaltered rocks of the Huincul Formation and the main structures were mapped at a scale of 1:25,000. Exposures of the sedimentary succession were studied in the walls of the two plateaus, where 5 representative stratigraphic sections were measured. Lithofacies characterization and architectural elements were based mainly on the classification of Miall (1996). Color variations were catalogued using a Munsell rock color chart. Representative samples of mineralized, altered, and unaltered rocks from the selected profiles were collected for laboratory analysis. Samples (n = 120) were analysed first with a binocular polarizing microscope under transmitted and reflected light. Based on these observations, consecutive samples along 5 profiles (n = 71, Fig. A.1–5) were selected for detailed laboratory analyses. Samples were representative of the mineralized, altered, and unaltered rocks from the Huincul Formation in the Tordillos area. Samples were analysed with a polarization-fluorescence Nikon Eclipse 50i microscope in order to detect organic compounds in diagenetic minerals. Modal mineralogy was determined by point counting (500 points) on each thin section of representative samples of unaltered and altered rocks. 2D image analyses were also used to obtain modal compositions and to quantify porosity using the software JMicroVision v.1.2.7 (Roduit, 2008). Clay mineralogy was determined by X-ray diffraction (XRD), infrared spectroscopy (IR) and scanning electron microscopy (SEM/EDX) at the IC2MP Laboratory at the Université de Poitiers (France). Due to the poorly consolidated state of the samples, sandstones were gently disaggregated in water, and the clay fraction was taken into suspension by ultrasonic treatment. Clay-size fractions
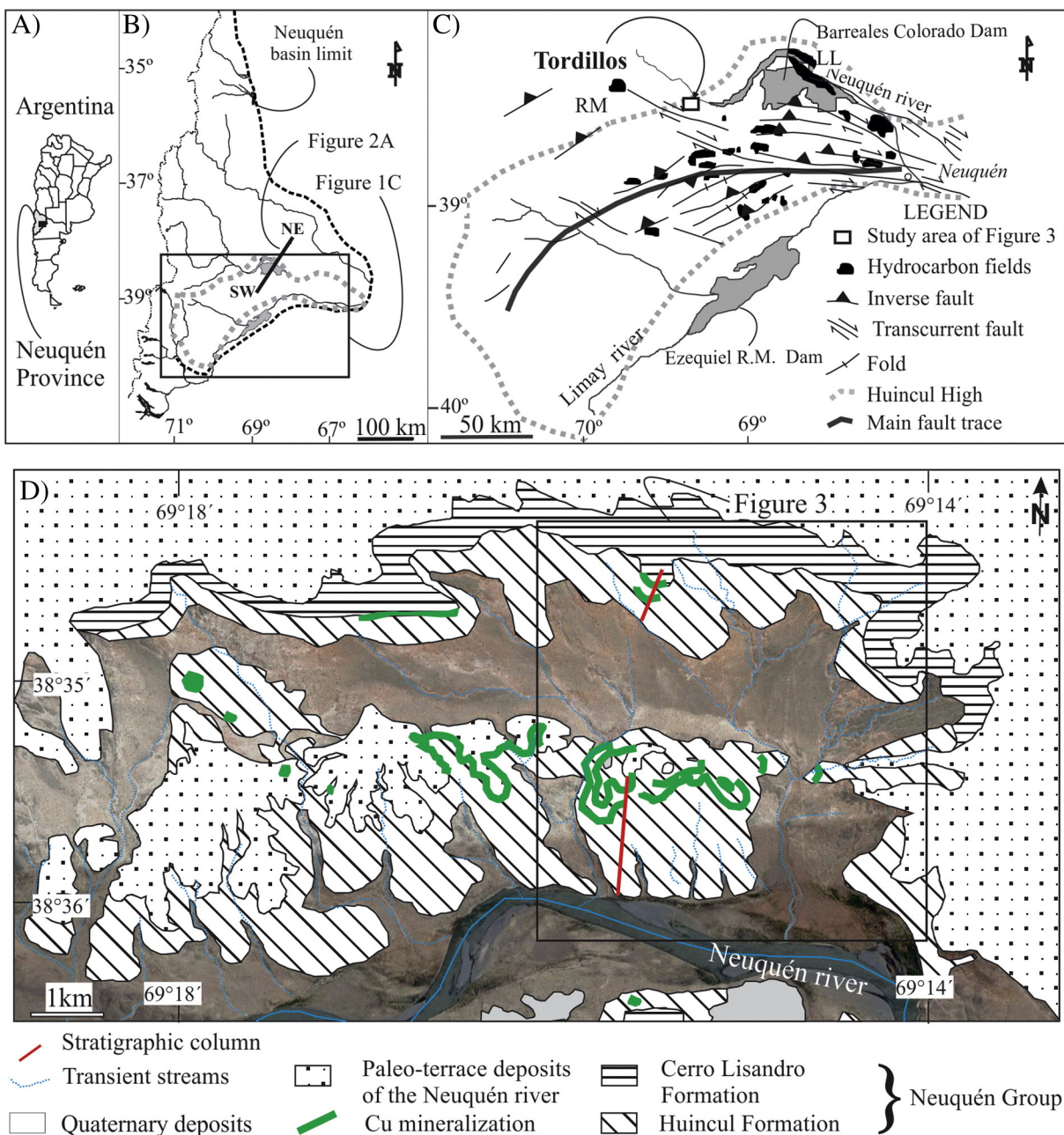
Fig. 1. A) Argentina map with the site of the Neuquén basin. B) Map of the Neuquén basin showing the location of the Huincul High and the hydrocarbon fields (modified from Giusiano and Bouhier, 2009). C) Structures and oil fields in the Huincul High and the location of the Tordillos deposit (modified from Silvestro and Zubiri, 2008). D) Geologic map of the Tordillos deposit (modified from Leanza et al., 2005). LL: Loma la Lata oil field RM: Rincón del Mangrullo oil field.

(<2 and <4 μm) were extracted by sedimentation for oriented and randomly oriented powder mounts. Only some problematic samples were treated with Ca saturation. All clay preparations were analyzed on a Bruker D8 Advance diffractometer. Diffracted beam radiation (CuKα1 + 2; 40 kV, 40 mA) was collected by a Lynx Eye detector. Relative humidity was not controlled during data acquisition. Quantitative clay analyses were carried out using the mineral intensity factor (MIF) method (Moore and Reynolds, 1997).

Infrared analyses were carried out on selected samples as a complementary technique for the determination of clay mineralogy. Middle-infrared (MIR) spectra (400 to 4000 cm^{-1}) were acquired from KBr pellets using a Nicolet 760 (Fourier Transformation Infrared Spectroscopy -FTIR-) spectrometer equipped with a potassium bromide (KBr) beam splitter and DTGS-KBr detector. The resolution was set at 4 cm^{-1} with co-addition of 100 scans. The KBr pellets were prepared using 1 mg of sample for 150 mg of KBr powder. The mixture was crushed in a mortar and placed in a hydraulic press for 5 min (<8 tons) before drying at 120 °C.

Seven thin sections of representative sandstones and mudstones with abundant carbonate cement were selected for cathodoluminescence analyses using a cold cathode (CL8200mk3) coupled to a Nikon Labophot microscope with vacuum chamber on the stage.

Representative samples of unaltered and altered rock were selected for scanning electron microscope (SEM) observations, which were done on carbon-coated thin sections and fragments of rock samples. Chemical compositions and the textures of clay minerals, calcite, and hematite, were studied using a JEOL® 5600 electron microscope equipped with a Bruker energy dispersive X-ray spectroscopy detector (EDX). Analytical conditions were: accelerating voltage 15 kV, probe current 1 nA, working distance 17 mm, counting time of 60 s. The elements analysed
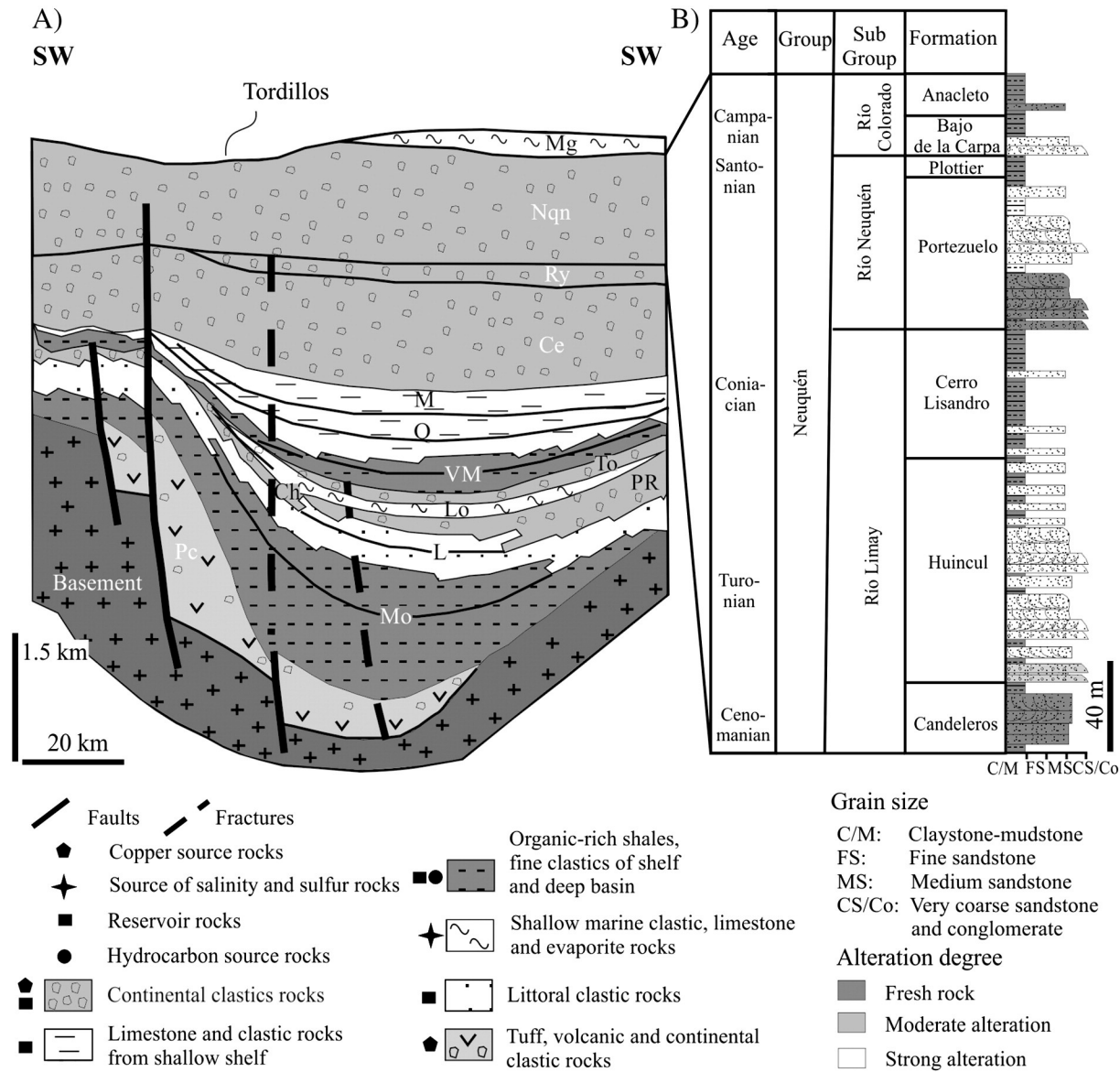
Fig. 2. (A) Northeast–southwest cross-section showing the stratigraphic succession of the Neuquén Basin with the Paleozoic (granitic basement); Triassic (Pre-Cuyo Formation; Pc), Jurassic (205–142 Ma: Los Molles [Mo], Lajas [L], Challacó [Ch], Punta Rosada [PR], Lotena [Lo], Tordillo [To] Formations), Cretaceous (142–65 Ma: Vaca Muerta [VM], Quintuco [Q], Mulichinco [M] Centenario [Ce], Rayoso [Ry] Formations and Neuquén [Nqn] and Malargüe [Mg] Groups) rocks and the main structures of the Huincul High (modified from Cruz et al., 2002). (B) Detailed stratigraphic column of the Neuquén Group (modified from Giusiano et al., 2008)

were Na, Mg, Al, Si, Mn, Fe, Ti, K, Ca, and Cu. SEM/EDX was considered more appropriate than electron microprobe analyses for the chemical compositions of fine-grained particles because the diameter of the electron-matter interaction is close to 1 μm. SEM/EDX also permits simultaneous analysis of all chemical elements of interest. The EDX analyses were calibrated using synthetic and natural oxides and silicates ($MnTiO_3$, hematite, albite, orthoclase, and diopside), with corrections made using a ZAF program. The relative errors on the analysed values are <1.5% (except for Na, for which the error is >3%).

Sulfide, sulfates and chrysocolla coatings were analysed at the Universidad de Barcelona by electron microprobe (Cameca SX-50) equipped with five wavelength dispersive spectrometers (WDS) and one energy dispersive spectrometer (EDS) silicon drift type detector (SDD), and at the New Brunswick University with a Superprobe JXA JEOL-733 in wavelength-dispersion mode, with 15 kV accelerating voltage, 10 nA beam current, and a maximum 40 s counting interval.

Representative samples (n = 26) of diagenetic, alteration and mineralization stages were analysed for major and trace elements using the ICP-ICP/MS facility at the Acmelab Analytical Laboratory, Canada.

4. Results

4.1. Local geology and description of stratigraphic units

Tordillos is located at the north-central limit of the Huincul High and on the SW flank of the Sauzal Bonito anticline, near the Loma la Lata (LL) and Rincón del Mangrullo (RM) hydrocarbon fields (Fig 1C). This fold was formed during the Jurassic-Cretaceous by tectonic inversion of the previous normal faults of Triassic rifting that were reactivated during the Tertiary Andean orogeny (Maretto and Pángaro, 2005).

North of the Neuquén River, the lower, middle and upper sections of the Huincul Formation (75 m thick; Upper Cenomanian, Herrero Ducloux, 1946; Ramos, 1981) and the base of the Cerro Lisandro Formation (35 m thick; Early Turonian, Herrero Ducloux, 1939; Leanza and Hugo, 1997 (Figs. 1D, 3 and 4) crop out. These redbeds, representative of the lower section of the Neuquén Group (Cenomamiano-Campanian, Garrido, 2011, and references therein; Figs. 1B, 2A, B), are unconformably covered by the paleo-

terrace deposits of the Neuquén River and Quaternary deposits (Fig. 1D).

The lower and upper sections of the Huincul Formation consist of a thinning- and fining-upward succession of medium-grained sandstones and clast-supported conglomerates (0.2–2.5 m thick) intercalated with fine-grained micaceous sandstone, mudstone and subordinate claystone layers (1–5 m thick; Figs. 1, 3, 4A, B). The sandstones and conglomerates are lenticular with medium-scale trough cross-bedding and a flat erosive base; these sedimentary rocks commonly contain fossil fragments of tree trunks and vertebrate bones (Figs. 3B, 4A). Planar stratification and lamination dominates in the finest facies, but thicker beds (4–5 m) are typically massive and show block fractures and claystone slickenside structures (Fig. 3B).

The middle section of the Huincul Formation is formed of stacked beds of sandstone and conglomerate with normal gradations and variable thicknesses (1 to 4 m, Fig. 4). The base of the strata hosts fossil bones and fragments of fossil tree trunks of varying sizes (up to 3 m long and 0.1 m wide), some oriented according to local paleo-current trends (N215°–N240°). The main structures are trough cross-bedding with paleo-current indicators (between N190° and N340°) and erosive bases with flat to concave surfaces. Some sandstone stratas have epsilon-type cross-bedding. An increase of fine-grained micaceous sandstones with ascending ripple marks and laminar mudstones occurs towards the top of this section (Fig. 3B).

The Huincul and Cerro Lisandro formations dip 4 to 6° to the northeast and form part of the northern flank of an anticline that crops out
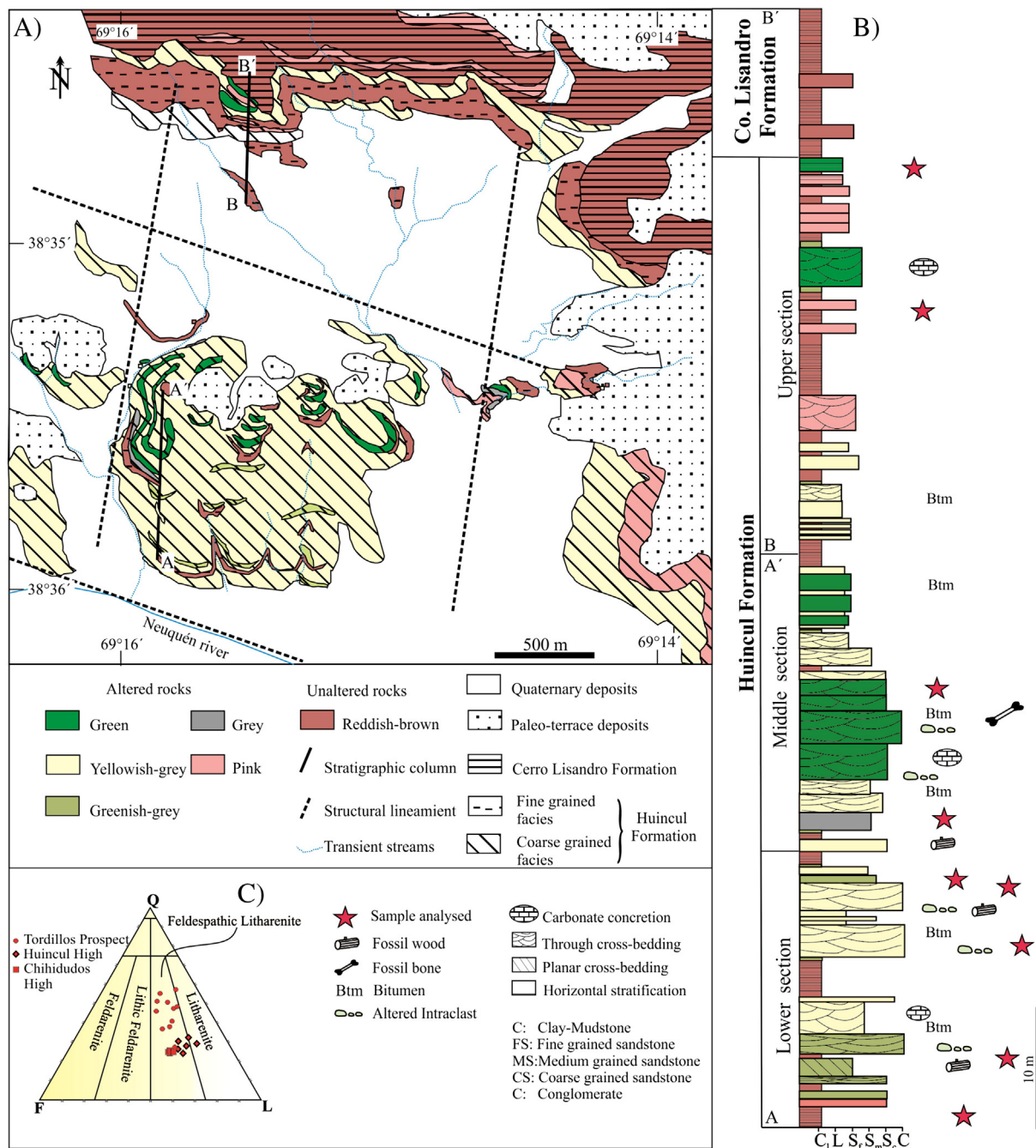
Fig. 3. A) Geological map showing the location of altered and unaltered rocks in the Huincul and Cerro Lisandro Formations. B) Stratigraphic profile showing the distribution of the reddish-brown, grey, greenish-grey, yellowish-grey and green rocks in Huincul and Cerro Lisandro Formations. C) Typical detrital mineralogy of sandstones from the Huincul Formation classified according Folk et al. (1970). (For interpretation of the references to color in this figure, the reader is referred to the web version of this article.)
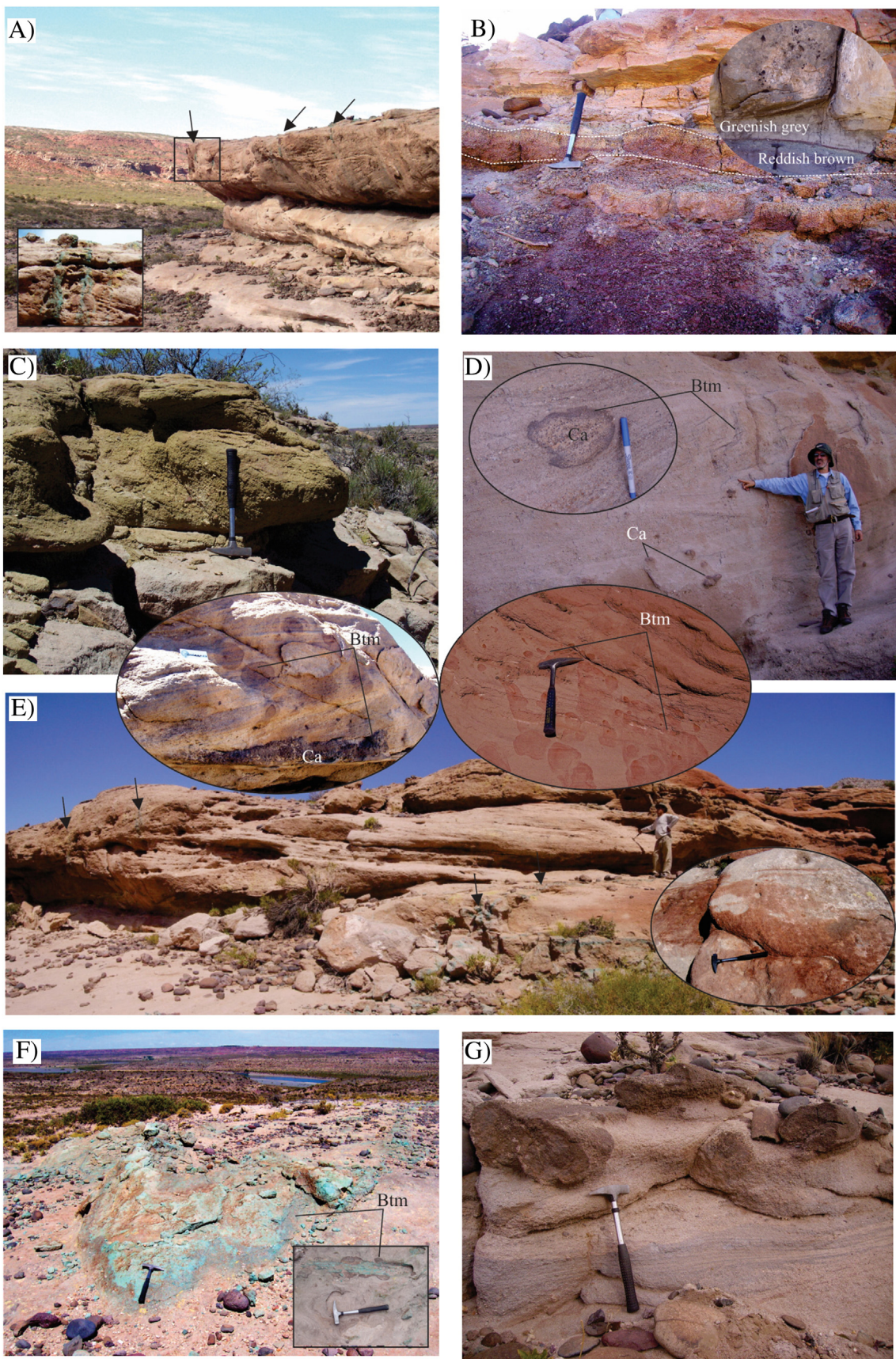
south of the study area. There are major lineaments with ENE and WNW trends, two NNE lineaments that delimited the central area of the project to the east and west (Fig. 1D), and a set of subordinate NW and

NS lineaments located south of the mineralized zone. The intersections of the major lineaments south of the study area correlate with an abrupt change in the orientation of the valley of the Neuquén River. The

Huincul Formation has numerous sub-vertical joints with variable trends (118–210° N and 265–310° N).

Petrographically, coarse-grained facies of the Huincul Formation have a moderate to poor sorting and contain clasts of monocrystalline and polycrystalline quartz (25 to 57%), volcanic, plutonic, sedimentary, and metamorphic (micaceous schists) lithics (29 to 47%), feldspar (10 to 24%), and minor amounts of micas, tourmaline, opaques (magnetite, rutiles), and zircon as accessories. Some pyroxene and amphibole grains were observed in the lower section (Table 1). Quartz clasts exhibit flash extinction and subordinate foliated and non-foliated polycrystalline aggregates. Most volcanic lithics are felsic to intermediate in composition and exhibit devitrification textures (spherulites and feathery axiolitic groundmass). Some volcanic fragments show a pilotaxic micro-porphyritic texture and microlithic groundmass, with deformed and altered fiammes that typically form the pseudomatrix. Plutonic lithics are composed of quartz and alkali feldspar with graphic and perthite textures. Sedimentary lithics are mudchips concentrated in conglomerates at the base of the paleo-channels. The samples analysed corresponded to lithic conglomerates and subordinate feldspathic litharenite and litharenite (Folk et al., 1970; Fig. 3C) typical of provenance from a recycled orogen (Dickinson et al., 1983). Quartz fragments are low in abundance in the lower section and basal middle section of the Huincul Formation (Fig. 3C; Table 1).

The mudstone facies consists of 48–54% clay, 24–29% quartz, 16–18% plagioclase, and 6–8% potassic feldspar, as well as phyllosilicates as inherited alteration minerals. Illite-smectite mixed layers were recognized by a characteristic superstructure near 25 Å in air-dried state which shifts near 27 Å after ethylene-glycol solvation (Figs. A.1–3).

All sedimentary rocks show evidences of mechanical compaction with slightly ductile deformation of the micas, volcanic lithics, and mud chips, forming pseudomatrix and brittle clasts with randomly oriented fractures.

4.2. Unaltered rocks of the Huincul Formation

The original reddish sedimentary rocks are only preserved in the reddish-brown mudstones of the lower and upper sections of the Huincul Formation that crop out south and north of the study area, respectively (Figs. 3, 4B). These mudstones are cemented by hematite coatings along with pore-filling kaolinite (7.2–19%), calcite (Fig. 5A), and gypsum (Fig. 6A). The top of the reddish-brown mudstones consists of a pervasive, 15–24 cm thick, carbonate-cemented layer (84 vol.%; Fig. 4B) composed of spherulitic red luminescent calcite1 (Fig. 5A-B) that has bioturbation channel structures.

4.3. Alteration of the Huincul Formation

Mineralized zones are enclosed in a large alteration halo (6 km long, 1.5 km wide and 10–20 m thick) which consists of intensively altered sandstones and conglomerates that exhibit color variations from yellowish-grey, pink, greenish-grey to grey base on the presence or absence of some epigenetic minerals (Table 2).

The yellowish-grey zone (Figs. 3, 4A, C, D) is widespread and particularly well developed in the coarse-grained rocks of the middle section of the Huincul Formation (Fig. 3A, B). The resulting yellowish-grey rocks are devoid of hematite coating and contain bitumen impregnations.

Altered sandstones turn dark when bitumen is abundant (Fig. 4D-E, G). Bitumen is concentrated in cross bedding, in disseminated spots, as subhorizontal flames with "V" and cylindrical shapes with variable trends (N285°-N200°), and as vertical tubes that crosscut the stratification (Fig. 4D). In contact with carbonate concretions (Fig. 4D), bitumen exhibits a dendritic pattern. At microscopic scales, bitumen coats grains and fractures and is systematically associated with traces of fine grained anhedral pyrite. Vermicular kaolinite replaces feldspar and volcanic lithics and fills the pore spaces (Figs. 7A, 8). At high magnification, individual kaolinite crystals show corroded edges and partial replacement by smectite (Fig. 7A). Smectite also rims clasts and contains hematite pseudomorphous after pyrite (Fig. 7B). Incipient meso-quartz overgrowths (>10 μm thick) developed upon some detrital quartz grains that lack smectite rims. The porosity of yellowish-grey sandstones and conglomerates which are not cemented by calcite ranges from 8 to 24% (Table 1), whereas the porosity of these sandstones cemented by carbonate ranges from 2 to 4%.

Four types of calcite were recognized based on their texture, relative chronology, and luminescence: 1) spherulitic calcite with red luminescence and replacing the vegetal structures of fossil logs along with interstitial micro quartz with cellular texture (Fig. 8A-B), 2) poikilotopic, white calcite with red luminescence and forming the core of rounded concretions or tabular and vertical tubes (Figs. 4D, 8C-D); 3) poikilotopic, fibro-radial calcite cement occluding the sandstones porosity, and 4) sparry calcite forming the external zones of the concretions. Calcite3 and 4 show orange to yellowish luminescences and host abundant organic fluid inclusions associated with euhedral or framboidal pyrite (<50 μm size) and bitumen (Fig. 8D).

Pink, fine-grained sandstones (Fig. 3A, B) with a representative porosity of 17% (Table 1) crop out in the upper section of the Huincul Formation, close to the contact with the Cerro Lisandro Formation (Fig. 3A, B). These sandstones contain smectite with interstitial barite (barite1) and bitumen coatings, and relics of kaolinite. Sparry calcite4 fills macropores locally (Fig. 7C).

Individual beds of greenish-grey sandstones and conglomerates (1.5 to 2.5 m thick; Figs. 3A, B, 4C) have been observed close to the contact with the reddish-brown mudstones and in the lower section of the Huincul Formation. The porosity in these greenish-grey sandstones varies from 11 to 16% (Table 1). The detrital grains of these rocks are pervasively cemented by 2 to 10 μm thick coatings of smectite and chlorite-like minerals (Fig. 9A-C) which are the cause of the greenish-grey hue. Smectite is partially replaced by chlorite-like crystals. Intergranular pore spaces, where the clay coating is absent, are cemented by incipient euhedral syntaxial micro (<10 μm; Fig. 9B) to meso-quartz overgrowths (20 μm; 1 < vol.%; Fig. 9D-E). Thin coating of bitumen, pyrite, and Mn-rich oxides occurs between grains and previous cements. The rocks have some irregular patches of late sparry calcite4 with bright orange to yellow luminescence and inclusions of pyrite (Fig. 9E, F). Similar feature affected reddish-brown mudstones close to the contact with altered sandstones (Fig. 3B) which are greenish-grey in colour over a few centimetres (<5 cm). Similar greenish-grey colorings were observed in the mud-chips at the base of paleo-channels from the middle and lower sections of the Huincul Formation. Greenish-grey mudstones (Fig. 4B) differ from the reddish-brown mudstones by the absence of the hematite and the presence of bitumen, as well as traces of chlorite (Fig. 6A, B). When these altered mudstones have carbonate cement, a

Fig. 4. Photographs of outcrops of unaltered, altered and mineralized rocks. A) The foreground shows typical paleo-channels in the middle section of Huincul Formation; in the back, the upper section of Huincul Formation and its contact with the reddish-brown mudstones of the Cerro Lisandro Formation. The black arrows point to vertical tubes containing copper mineralization square show a detailed of copper tubes. B) Reddish-brown mudstones from the Huincul Formation grading upward to a pervasively calcite-cemented layer. The oval shows a detail of the contacts among reddish-brown mudstones, greenish-grey mudstones, and yellowish-grey sandstones. C) Greenish-grey conglomerates from the lower section of the Huincul Formation. D) Yellowish-grey sandstones with bitumen (Btm) impregnations, and calcite concretions (Ca). E) Copper mineralized hydrocarbons tubes (black arrows) in the yellowish-grey sandstones. The three ovals show details: of bitumen impregnation in yellowish-grey sandstones (upper left), bitumen and oxidation halos after pyrite (upper right) and irregular iron oxides (oval bottom right). F) Mineralized flame structure in contact with bitumen, chalcocite group minerals are distinguished by their grey colors and supergene copper minerals by their light bluish and greenish colors. In the inset (bottom right), a fossil trunk is replaced by copper mineralization at the contact with bitumen. G) Grey sandstones beneath greenish sandstones in the middle section of the Huincul Formation. (For interpretation of the references to color in this figure, the reader is referred to the web version of this article.)

Table 1
Detrital grains, diagenetic minerals, and porosity in sandstones of the Huincul Formation.

Color	Pink	Yellowish-grey	Yellowish-grey	Py-rich-yellowish grey	Py-rich yellowish grey	Yellowish-grey chrys	Yellowish-grey chrys	Yellowish-grey chrys	Greenish-gray	Greenish-grey	Grey	Green
Sample number	To 140409-20	To 140209-3	To 11108-7D	To 21107-9	To 21107-1	To 140209-12b	To 140209-9	To 21107-5	To 140209-6	To 111209-7	To 21107-10	To 21107-14b
Qz	37.50	35.00	34.70	33.60	31.25	32.25	28.39	26.50	1.84	20.10	23.26	24.31
Qz1	1.00	3.00	0.00	3.60	2.00	2.00	2.08	1.00	12.34	3.90	0.00	0.00
Qz2	0.50	1.25	0.00	1.00	3.25	0.50	1.04	1.00	0.16	0.22	6.85	0.31
Qz3	1.25	10.50	1.78	9.20	6.50	7.50	5.99	9.00	6.94	6.93	2.14	0.00
Pl	10.25	4.50	2.31	5.40	5.50	3.50	6.77	3.75	10.00	2.81	5.70	5.85
Afs	10.75	3.50	9.79	9.80	8.75	10.00	10.94	6.50	9.05	14.29	13.54	4.00
Aafs	0.00	0.25	3.74	0.00	0.00	0.00	0.00	0.00	0.00	4.55	0.00	7.69
M - Micas	5.50	0.00	0.00	0.00	0.00	0.50	0.00	0.25	0.00	0.00	0.00	0.00
Op - Opacos	0.50	0.00	0.53	0.00	0.75	0.00	0.52	0.25	0.00	0.22	0.28	0.00
La	7.75	0.25	7.12	1.00	5.50	5.50	0.26	3.00	0.31	1.52	2.43	5.23
Lm	0.50	1.25	0.00	2.00	2.50	1.25	1.04	2.75	0.00	0.00	0.00	0.00
Lp	0.00	0.75	1.07	0.00	0.00	0.00	0.00	0.00	0.47	1.08	5.85	4.62
Lpv	13.25	25.50	6.95	18.40	16.25	23.00	31.77	22.50	35.30	26.44	16.56	12.62
Ls	4.00	0.50	4.27	0.60	2.50	2.50	2.08	0.50	0.00	1.30	0.00	0.31
Co	0.75	0.25	0.71	0	0.75	0.50	0.78	10.00	0.47	0.65	0.00	0.00
Cb	0.75	5.75	0.00	12.20	1.75	3.25	0.00	0.00	0.00	0.00	0.00	0.00
Cl	1.50	3.75	0.00	1.00	2.75	0.75	2.08	8.50	5.40	4.11	1.28	16.92
Ps	0.00	0.00	2.49	1.00	0.00	0.50	0.00	4.50	1.70	0.22	0.00	0.31
P	4.25	4.00	24.56	0.40	8.50	6.50	6.25	0.00	16.04	11.69	20.84	0.00
Ci	0.00	0.00	0.00	0.80	1.50	0.00	0.00	0.00	0.00	0.00	0.00	0.00
Cc	0.00	0.00	0.00	0.00	0.00	0.00	0.00	0.00	0.00	0.00	0.00	17.85
Total	100.00	100.00	100.02	100.00	100.00	100.00	100.00	100.00	100.00	100.00	100.00	100.02
Qz	40.25	49.75	36.48	47.40	43.00	42.25	37.50	37.50	21.28	31.15	32.25	24.62
Fsp	21.00	8.25	15.84	15.20	14.25	13.50	17.71	10.25	19.05	21.65	19.25	17.54
Lt	25.50	28.25	19.41	22.00	26.75	32.25	35.16	28.75	36.07	30.34	24.83	22.78
Total	86.75	86.25	71.73	84.60	84.00	88.00	90.36	76.50	76.41	83.14	76.32	64.94
Qz	46.40	57.68	50.86	56.03	51.19	48.01	41.50	49.02	27.86	37.47	42.25	37.91
Fsp	24.21	9.57	22.08	17.97	16.96	15.34	19.60	13.40	24.94	26.04	25.22	27.01
Lt	29.39	32.75	27.06	26.00	31.85	36.65	38.90	37.58	47.21	36.49	32.53	35.08
Recalculate to 100%	100.00	100.00	100.00	100.00	100.00	100.00	100.00	100.00	100.00	100.00	100.00	100.00

Aafs = alterated alkali feldspar; Afs = alkaline feldspar; Cb = carbonates cement; Cc = chalcocite; Ci: iron oxides cements; Cl = clay cement; Co = other cements; La = alterated minerals; Lm = metamorphic lithic grains; Ps = pseudomatrix; Lp = plutonic lithic grains; Lpv = paleovolcanic lithic grains; Ls = sedimentary lithic grains; Ms = mica grains; Op = opaque mineral grains; Pl = plagioclase; P = porosity; Ps = pseudomatrix; Qz1 = polycrystalline quartz with two subgrains; Qz2 = polycrystalline quartz with three subgrains; Qz3 = polycrystalline quartz with more than three subgrains. Recalculated values = Qz = Qz + Qz1 + Qz2 + Qz3; Fsp = Pl + Afs + Aafs; Lt = La + Lm + Lp + Lpv + Ls.

brown-red luminescent calcite1 is replaced by a bright orange luminescent calcite4 along cleavage or as microveinlets (Fig. 5A-B), accompanied by pyrite and bitumen impregnations.

Grey sandstone layers (1 to 2 m thick) occur at the contact between the mineralized zone and yellowish-grey rocks and above the reddish-brown mudstone layer west of the central zone (Figs. 3A,B; 4G). Other small outcrops of grey sandstones were also observed at the contact between green and pink sandstones to the east (Fig. 3A). The grey sandstones have high porosity (20.8%; Table 1) and show regular coatings of detrital grains by smectite associated with hexagonal platy crystals

of vanadium-bearing hematite (with crystal diameters up to 3 µm; Fig. 9G, H). Calcite cements are rare; relics of kaolinite were detected in some samples.

4.4. Mineralization of the Huincul Formation

The copper mineralization is hosted mainly in the middle section of the Huincul Formation and consists of iron-copper and copper sulfides and supergene minerals. They follow the main paleo-channels (Fig. 4A, E, F) and fluid-escape structures (e g. bitumen tubes; flames; see
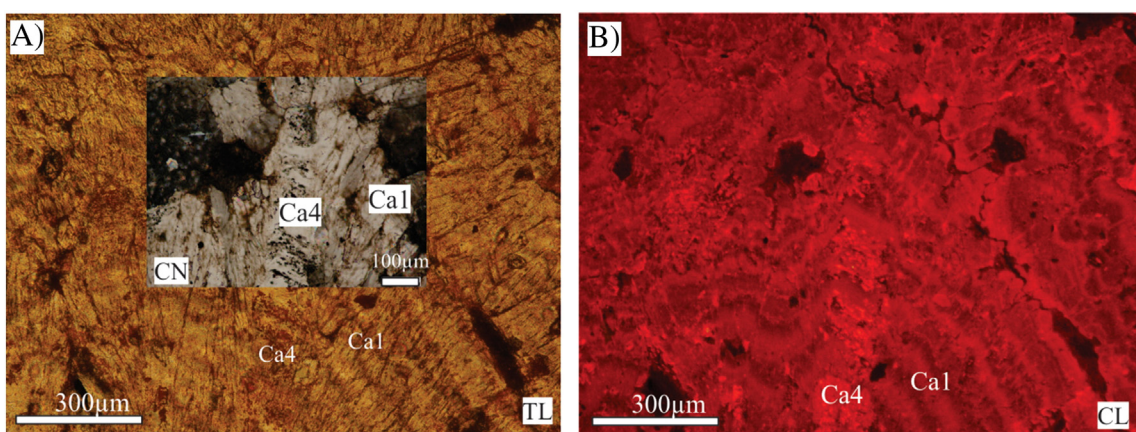

Fig. 5. Photomicrographs A–B) of fibro-radial calcite1 (Ca1) cut by veins of calcite4 in mudstones. CN: crossed nicols; CL: cathodoluminescence image; TL: transmitted light.
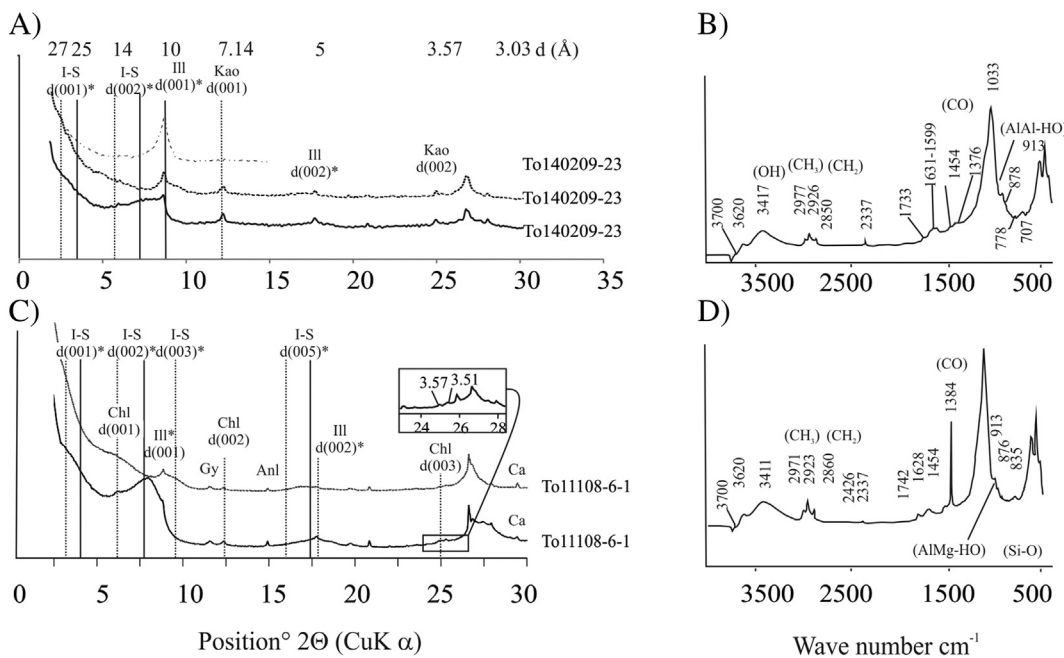
Fig. 6. X-ray diffraction patterns and FTIR spectra representative of clay fraction samples. A–B) reddish brown and C–D) greenish grey mudstones from the Huincul Formation, showing traces of inherited (*) I-S mixed layers and illite and authigenic kaolinite and chlorite. In the X-ray diffraction pattern the solid line represents air-dried samples, dotted line samples after ethylene glycol solvation, and the dashed line sample after 550 °C calcination. Ca: calcite; Chl: chlorite; Ill: illite; Kao: kaolinite; Qz: quartz; Plg: plagioclase; I-S: illite-smectite mixed layers.

Figs. 3, 4A, F). Iron-copper and copper minerals are always in contact with bitumen, hence, in outcrops they show similar patterns described for bitumen (Fig. 4A, F). The mineralized sandstones and conglomerates contain: a) relicts of barite1 coatings; b) coarse crystals of barite2 hosting abundant organic fluid inclusions and bitumen impregnations; and c) pyrite, all partially and totally replaced by traces of bornite and chalcopyrite and chalcocite group minerals (Fig. 10A-D). Chalcocite group minerals (digenite to anilite) are the most widespread and abundant sulfides cementing the sandstones and conglomerates. Veinlets of barite3 cut the sulfides and early cements.

4.4.1. Supergene alteration

The green color of these rocks is due to the supergene Cu and U-V minerals that replace the hypogene sulfides. Covellite replaces iron copper and copper sulfides and grades to brochantite, tenorite, and cuprite toward the contact with bitumen coatings. Efflorescences of volborthite,

carnotite, and francevillite with relicts of sulfides and brochantite occur between bitumen and barite2 (Pons et al., 2014). The latest and more abundant supergene mineral is chrysocolla. Less commonly, malachite ± azurite occur at the contact between the sandstone and silicified logs (Fig. 4F).

Close to the mineralized sandstones, the altered rocks show irregular iron oxide-rich halos cutting the sedimentary structures (Fig. 4E), with relicts of partially oxidized pyrite. Rosettes of hematite and iron oxi-hydroxide (e. g., goethite) overprint smectite and chlorite-like rims in the pink (Fig. 7E) and greenish-gray sandstones (Fig. 9C).

Common features of the mineralized rocks are the following: a) low porosities (<1%) generally occluded by copper minerals (Fig. 10D); b) subhorizontal and subparallel fractures filled with barite3, anhydrite and supergene copper minerals cut grains and diagenetic cements (Fig. 10A; C) a lower content of clay minerals compared with the other altered rocks (Figs. 11, 12); and d) quartz overgrowths at the

Table 2
Diagenetic, alteration and supergene minerals in sandstones and conglomerates of the Huincul Formation.

| Minerals-bitumen/color rock	Reddish-brown mudstone	Pink	Yellowish-grey	Py-rich yellowish-grey	Greenish-grey	Grey	Green
Hematite	x						
Kaolinite	x	x	x				
Calcite1	x						
Barite1		x					x
Gypsum	x						
Calcite2			x				
Bitumen			x	x	x		x
Pyrite		x	x	x	x		
Smecite	x	x	x			x	
Calcite3			x				
Calcite4	x	x					
Chlorite-like minerals					x		
Quartz overgrowth			x	x	x		
V-hematite						x	
Barite2							x
Chalcopyrite							x
Chalcocite group							x
Barite3							x
Supergene Cu minerals							x
Supergene iron-oxides and hydroxides	x		x		x		x
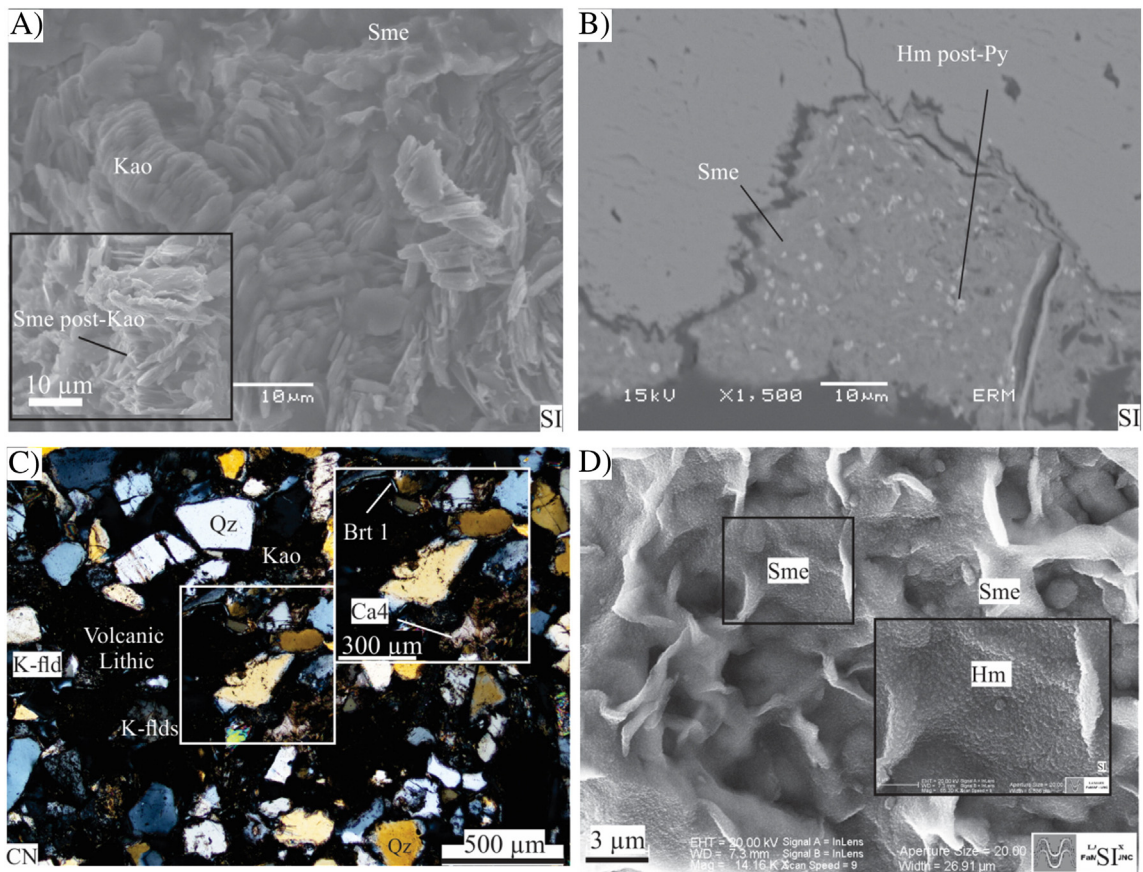
Fig. 7. Photomicrographs of authigenic and alteration minerals. A) Interstitial kaolinite with vermicular and book-like habits partially dissolved and replaced by smectite. B) Smectite rim, including micro-boxworks of pyrite in the yellowish-grey sandstones. C) Diagenetic and alteration cements of pink sandstones (see text for explanations). D) Detail of smectite covered by iron oxides in pink sandstones. Brt1: barite1; Ca1: calcite1; CN: cross nicols; Kao: kaolinite; Hm: hematite; K-fld: potassium feldspar; Ms: muscovite; Qz: quartz; TL: transmitted light; SI: SEM image; Sme: smectite. (For interpretation of the references to color in this figure, the reader is referred to the web version of this article.)

contact with copper minerals show corroded edges and embayments (Fig. 10B).

4.5. Characterization and compositions of minerals and organic matter

Representative analyses (XRD, MIR, and chemical) of clay, calcite, sulfate, sulfides, and iron oxides minerals are presented in Figs. 6, 11-14, A.1–5 and Tables 3-5, B.1–3. The structural formula for clay minerals was calculated on the basis of $O_{11}(OH)_8$ anion content (Newman and Brown, 1987). Iron from the yellowish-grey and greenish-grey rocks was calculated as Fe^{2+} in smectite and chlorite-like minerals where they coexist with pyrite and bitumen. Iron was calculated as Fe^{3+} in the smectite from the grey rocks where smectite is in contact with hematite. The structural formula of the various generations of barite (1 to 3) and brochantite were calculated on the basis of 4 oxygen (Table 4).

4.5.1. Diagenetic stage

Kaolinite has been identified in red mudstones and as relict mineral in altered sandstones and conglomerates from the X-ray diffraction and infrared spectra of fine-grained fractions (<5 μm) that show typical absorption bands at 3699, 3652, 795, 758, 697, 533, 472, and 426 cm^{-1} (Figs. 6B, D; 11B, D, F; 12 B, E, G). The presence of a doublet between 3669 and 3652 cm^{-1} (Figs. 11B, D, 12E) is indicative of the ordered structure of kaolinite (Russell and Fraser, 1994). The chemical composition of barite1 is $Ba_{0.52-1.06}Cu_{0.0-0.23}S_{0.51-0.96}O_4$ (Table 4).

4.5.2. Alteration stage

Smectite was identified in yellowish-grey, grey, and greenish-grey sandstones and conglomerates, based on a d(001) reflection close to 17 Å, and d(002) and d(003) reflections at 8.5 Å, and 5.67 Å, respectively after ethylene-glycol solvation (Figs. 11, 12) (Moore and Reynolds, 1997). FTIR analyses show an absorption band between 3624 and 3622 cm^{-1}, close to the typical OH-stretching band of the dioctahedral smectite (Madejová et al., 2011), and a broad band near 3420 cm^{-1} due to OH stretching vibrations of the adsorbed water of smectites (Fig. 11B, D, F). The band at approximately 914.4 cm^{-1} wave number indicates the presence of smectite having the AlAl-OH band (Madejová et al., 2011), and the shoulder at 841 cm^{-1} corresponds to the AlMg-OH deformation band (Fig. 11F).

The composition of the smectite is rather homogeneous and fits well with that of a dioctahedral aluminous smectite. The structural formula of this type of smectite is compatible with that of a montmorillonite (high Si content in tetrahedral layers and significant amount of divalent elements in octahedral layers). The only significant chemical variation of this smectite seems to be the amount and nature of the dominant cation in interlayer position which varies from one alteration site to another. For example, montmorillonite from the yellowish-grey sandstones in contact with the mineralized rocks has the highest interlayer occupancies and calcium content, and shows traces of copper (Fig. 13E; Table B.1). In the pyrite-rich yellowish-grey sandstones, montmorillonite shows the lowest proportion of interlayer cations and in the grey rocks it has traces of V (Fig. 13E; Table B.1). Other slight chemical variations could be due to minor amounts of mineral impurities (pyrite, iron oxide or ox-hydroxides, alkali feldspars or detrital micas).
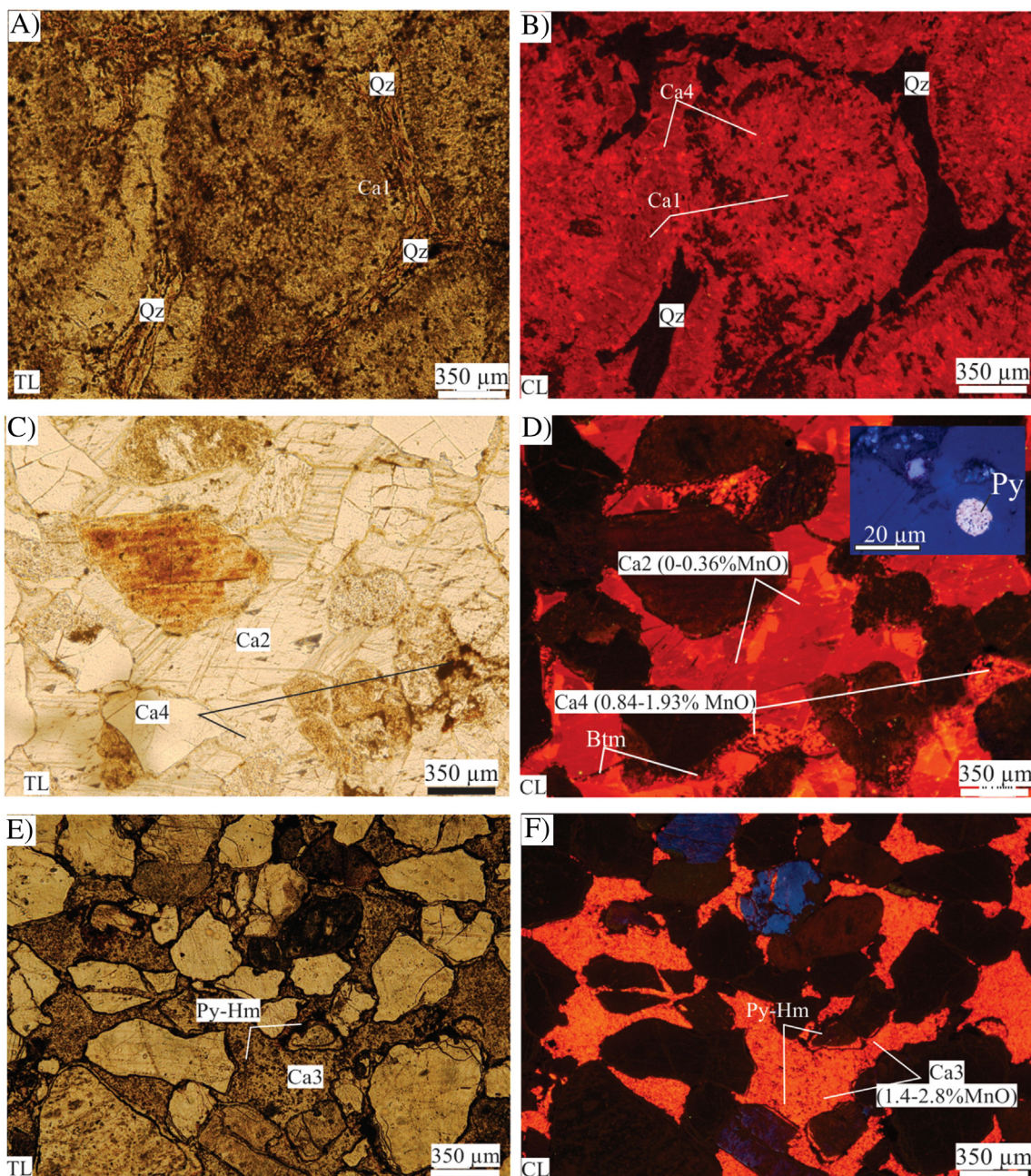
Fig. 8. A–F) Photomicrographs of carbonate cements in the yellowish-grey sandstones (see text for details). Ca1, 2, 3, 4: calcite1, 2, 3, 4; CN: cross nicols; CL: cathodoluminescence image; Hm: hematite; Qz: quartz; TL: transmitted light; SI: SEM image; Py: pyrite.

Mixtures of chlorite (chl) and chlorite-corrensite mixed layers (chl-cor) together with smectite were identified in the greenish-grey sandstones (Fig. 12A-C). The XRD patterns of the air-dried clay material differs from that of true chlorite in the following characteristics: 1) the higher intensity of the d(001) reflection and the relative weakness of the d(003) and d(004) reflections; 2) the weak asymmetry of diffraction peaks occurring near intense corrensite (cor) reflections (e.g., d(001)chl, d(002)cor; d(002)chl, d(004)cor; d(003)chl, d(006)cor, d(004)chl, and d(008)cor reflections). After ethylene glycol saturation, discrete smectite is identified from the 17Å reflection and its rational suborders in association with overlapped diffraction peaks whose behavior according to the swelling state is characteristic of a mixture of chlorite and chlorite-corrensite mixed layers. Mixture of chlorite and chlorite-corrensite can also be identified from the composite peak near the chlorite d(003) reflection (Fig.12C), which decreases in relative

intensity and broadens strongly but remains almost symmetrical for corrensite d(006) and d(007) reflections located at equal distances from the chlorite d(003) reflection after ethylene glycol saturation (see simulations in Beaufort et al., 1997). The major discrete chlorite peak present in this clay fraction represents the major phase and corresponds to poorly crystallized chlorite particles (FWHM = 0.70° 2θ CuKα) that are not consistent with impurities of residual metamorphic chlorite. FTIR spectra of this clay shows a broad band between 3624 cm^{-1} and 3566 cm^{-1} which could be explained by a mixture of dioctahedral smectite (normally 3622–3636 cm^{-1}) along with trioctahedral (Mg-Fe rich) chlorite like (3627–3540 cm^{-1}; Madejová et al., 2011; Fig. 12B).

The clay minerals analyzed in the greenish-grey rocks are characterized by a large compositional field that extends from ideal montmorillonite to ideal trioctahedral chlorite. Such a chemical trend is
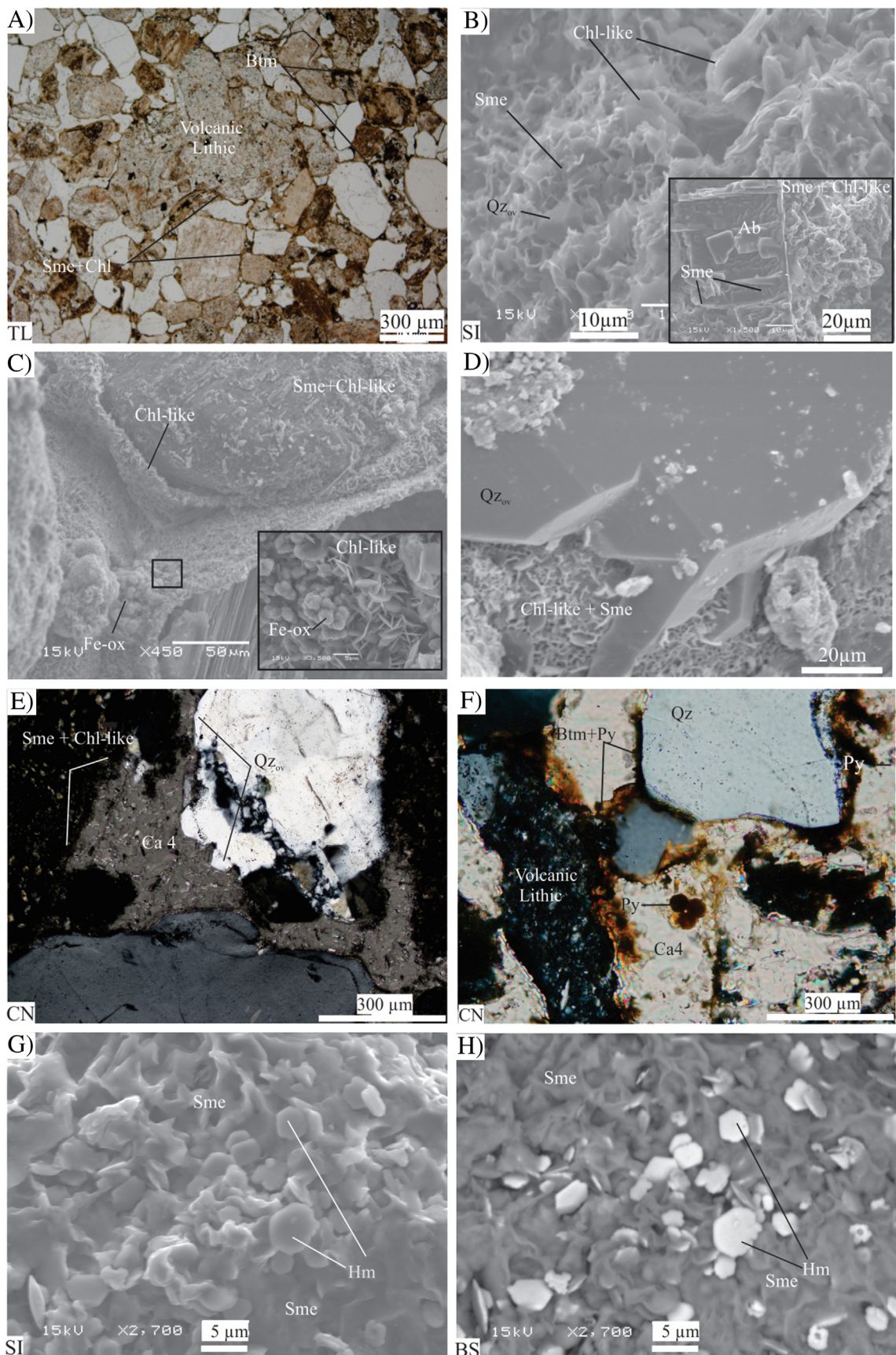
Fig. 9. Photomicrographs (A, E, and F) and scanning electron microscope images (B, C, D, G and H) documenting the texture of the authigenic minerals in the greenish-grey (A–F) and grey sandstones (G–H). See text for details. Ab: albite; Btm: bitumen; Ca: calcite1; Chl: chlorite; CN: crossed nicols; Fe-Ox: iron oxides; Hm: hematite; Kao: kaolinite; K-flds: potassium feldspar; Ms: muscovite; Py: pyrite; Qz$_{ov}$: quartz overgrowth; Sme: smectite. TL: transmitted light; SI: SEM image;.
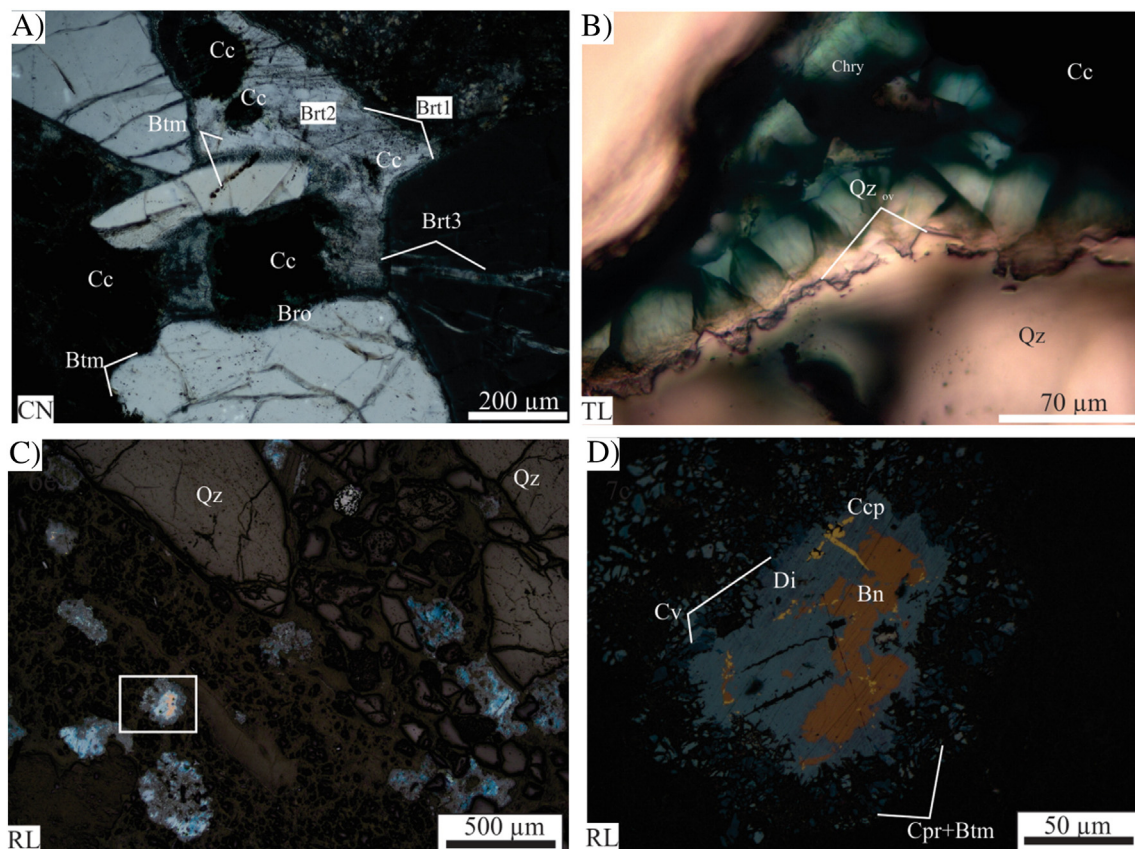
Fig. 10. A–D) Photomicrographs of the representative green sandstones with hypogene and supergene copper mineralization and several generations of barite (see text for details). Bn: bornite; Brt1, 2, 3; barite1, 2, 3; Bro: brochantite; Btm: bitumen; Cc: chalcocite group minerals; Ccp: chalcopyrite; Chry; chrysocolla; CN: crossed nicols; Cv: covellite; Cpr: cuprite; Di: digenite; TL: transmitted light; RL: reflected light;

illustrated in cross-plot diagrams which indicate that the ratios between Si, Al or Fe + Mg versus the calculated octahedral occupancy are highly variable but fall systematically between montmorillonite and chlorite (Fig. 13B-D). This chemical trend is indicative of mixture of chlorite and montmorillonite at the scale of the EDS analysis (electron beam focused to 1 μm). The absence of a significant deviation of the compositional field of the mineral mixture towards that of saponite (Fig. 13B-D) precludes the presence of this mineral and also suggests low amounts of corrensite in the chlorite-corrensite mixed-layer minerals identified by X-ray diffraction in the greenish-grey rocks.

Calcite generations 2, 3, and 4 from the altered rocks and the interstitial calcite from the greenish-grey sandstones contain MnO (0.002–4.75%; Fig. 14, Table B.2); furthermore, those with impregnations of bitumen have the highest MnO contents (2.5–4.75%; Fig. 8G-H). In these three types of calcite there is a negative correlation between CaO and MnO (Fig. 14). The spherulitic calcites (generations 1 to 4) also show a negative correlation between CaO and MgO and FeO dispersion (Fig. 14). The composition of tabular barite2 is $Ba_{0.98-1.37}Sr_{0.0-0.12}Cu_{0.0-0.11}S_{0.86-0.99}O_4$ (Table 4).

Hematite from the grey rocks is characterized by its significant vanadium (0.6–2.37%) and titanium (0.6–1.9%) contents and traces of manganese (0.2–0.6) (Table 5).

Organic matter was identified by FTIR spectra. All the samples show an intense band at the 2800 cm^{-1} region characteristic of traces of aliphatic groups (CH$_2$—CH$_3$ stretching vibrations; Figs. 6B, D; 11B, D, F; 12B, E, G). MIR spectra of all samples show three main absorption bands caused by a stretching bond in the COOH functional group, with the band close to 1700 cm^{-1} indicating the double bond of C═O, and a broad band centered in the range 2700–3300 cm^{-1} that could be caused by the presence of the O—H stretching bond (Figs. 6B, D; 11B,

D, F; 12B, E, G). The band near 1400 cm^{-1} could be due the bending vibration bond of O—H or C—H (Figs. 6B, D; 11B, D, F; 12B, E, G). Based on the spectra bands intensities, the pink sandstones show the lowest amount of organic matter. These results indicate that the kind of organic matter in analyzed samples is homogenous in all the altered rocks.

4.5.3. Mineralization stage

Chemical analyzes of copper sulfides show a range between digenite ($Cu_{4.6-5.04}S_{8.95-9.4}$) to anilite ($Cu_{6.98-7.12}S_{3.87-4.04}$) from core to rim and show traces of Mn, Ag, Zn, Mo and Pb (Table B.1). Detailed laser ablation ICP-MS studies in chalcocite group minerals confirmed the presence of Zn, V, Fe, Ag, Si, Mo and As elements in trace amounts.

Barite3 shows the lowest total oxides (<73.5%) in comparison with previous barite(1, 2) and has an intermediate composition between barite and brochantite ($Ba_{0.66-1.13}Cu_{0.21-0.76}Sr_{0.0-0.07}S_{0.77-0.94}O_4$; Table 4), probably due to the presence of micro-inclusion of brochantite within the barite.

4.5.4. Supergene stage

Covellite ($Cu_{0.98-1}S_{1-1.02}$) partially replaces chalcocite group minerals as paths or as external halos surrounding the previous sulfides and shows the same trace elements of their precursor (Table B.3).

Brochantite in contact with sulfides and barite shows traces of Ba ($Cu_{2.00-2.26}Ba_{0-0.08}S_{0.61-0.63}O_4 \cdot H_2O$; Table 4).

Chrysocolla is widespread in the mineralized sandstones and in the altered sandstones close to the main mineralized zone. It was identified in thin section and also by the presence of two peaks at 1.48 Å and 2.54 Å in XRD patterns. The structural formula of chrysocolla from the microprobe analyses was recalculated on the basis of 9 oxygens ($Cu_{0.98-2.45}$, $Al_{0.34-0.52}$)$H_{1.48-1.66}Si_{1.79-2.29}O_5(OH)_4nH_2O$ (Table 3). One
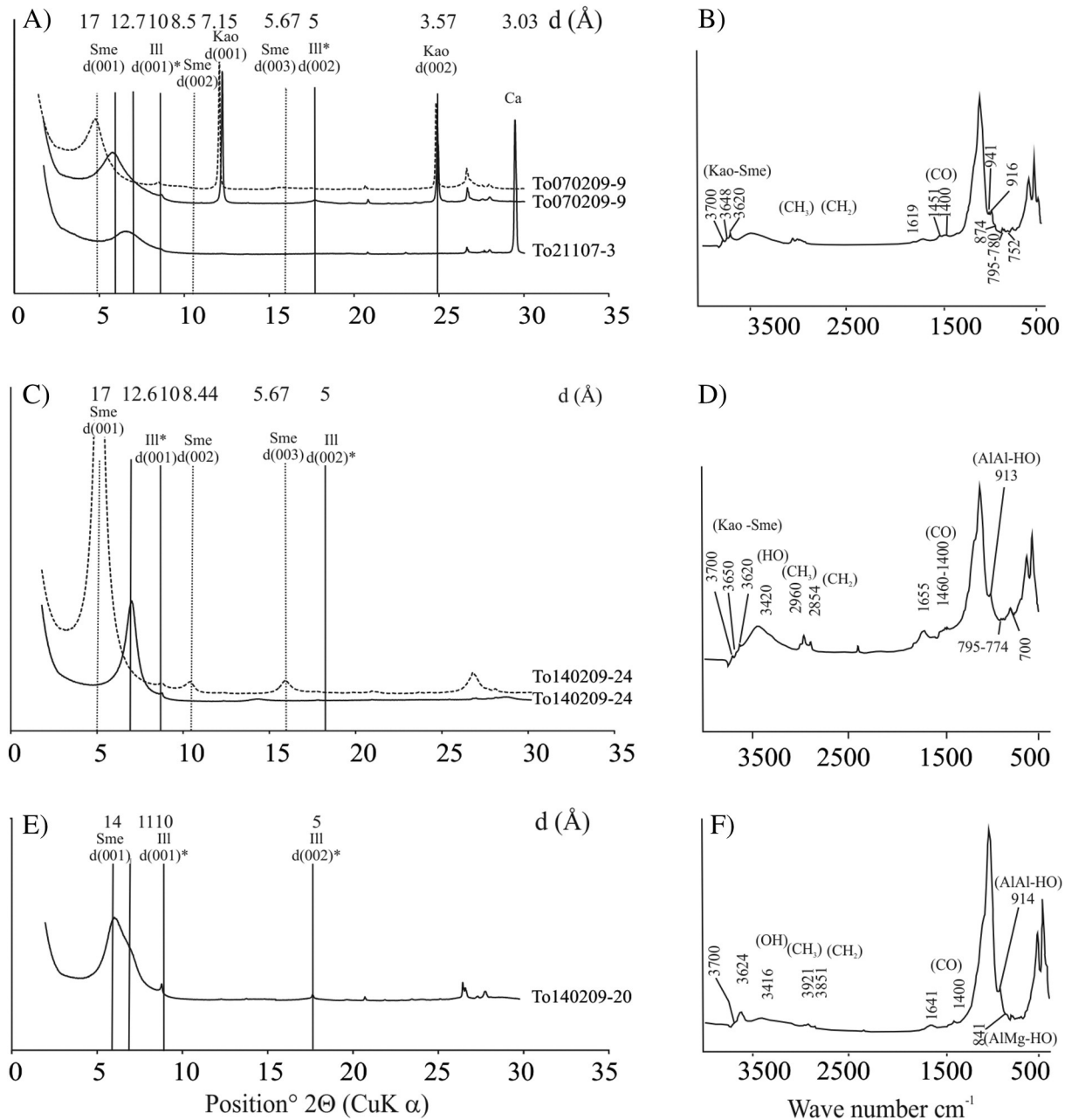
Fig. 11. X-ray diffraction patterns and FTIR spectra of representative clay fraction samples of A–B) yellowish-grey, C–D); pyrite-rich white and E–F) pink rocks (see text for details). In the X-ray diffraction patterns, the solid line represents air-dried samples and dotted line samples are after ethylene glycol solvation. Ca: calcite; Chl: chlorite; Ill: illite; Kao: kaolinite; Sme: smectite.

of the microprobe analyses corresponds to a Cu-rich smectite indicating a transition between smectite and chrysocolla (Table 3). The anomalous MnO content (up to 22.68% MnO) in the chrysocolla could be due the presence of fine MnO inclusions.

The supergene iron oxide from the altered rocks has manganese (<8%) with traces of V, Ti, Cu, S, and Cl (Table 5).

4.6. Geochemistry

Chemical data from the unaltered mudstone and altered rocks from the Huincul Formation shows variations in both major oxides and trace elements (Fig. 15; Table B.4). Major and trace elements distributions in the sandstones and mudstones are illustrated in

Harker-type diagrams with Fe_2O_{3total}, MgO, Al_2O_3, K_2O, Na_2O, CaO, MnO, Ba, Sr, Cu, V, and U plotted against SiO_2 (Fig. 15). Fe_2O_{3total}, MgO, and Al_2O_3 decrease as SiO_2 increases from the reddish-brown to the greenish-grey mudstones, and from the greenish-grey, to the pink, yellowish-grey and grey sandstones. Some green sandstones and one sample from the yellowish-grey rocks pervasively cemented by calcite show lowest SiO_2 values (Fig. 15). Reddish-brown mudstones show the highest $Fe_2O_{3\ total}$ contents (5.16 to 9.26%), whereas greenish-grey mudstones are depleted in 2 to 5.6% of Fe_2O_{3total} with respect to the iron content of reddish-brown mudstones. K_2O contents show dispersion in all samples analysed, with highest values present in mudstones. Na_2O increases with respect to SiO_2 from the reddish-brown to greenish-grey mudstones and some greenish-
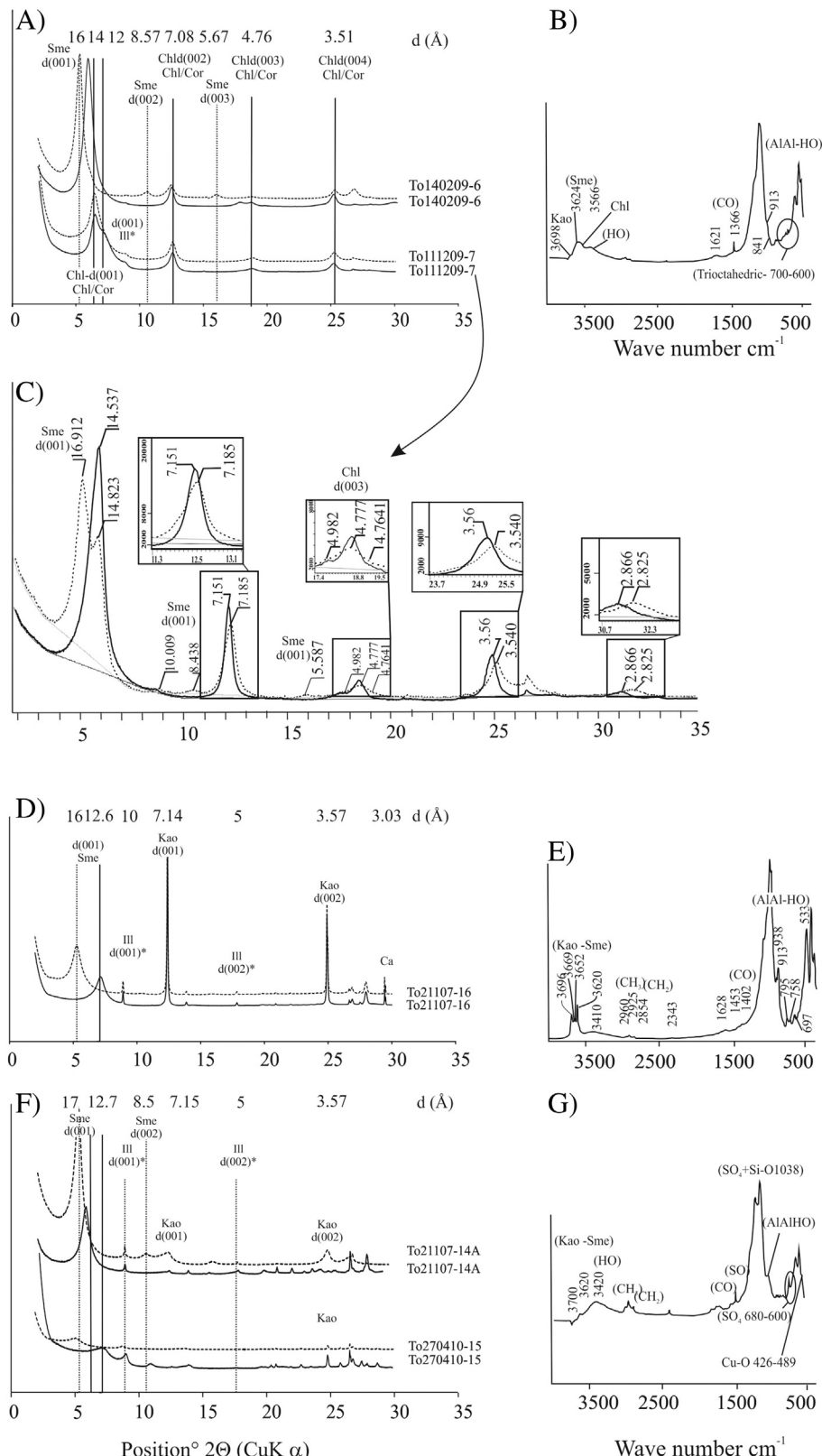
Fig. 12. X-ray diffraction patterns and FTIR spectra of representative clay fraction samples of A–C) greenish-grey, D–E) grey; F–G) green sandstones. In this last figure, the upper two diffractograms are from yellowish grey rocks in contact with mineralization, for comparison (see text for details). In the X-ray diffraction patterns, the solid line represents air-dried samples and dotted line samples are after ethylene glycol solvation and C) after calcium saturation (see text for details). Ca: calcite; Chl: chlorite; Ill: illite; Kao: kaolinite; Sme: smectite. (For interpretation of the references to color in this figure legend, the reader is referred to the web version of this article.)

grey sandstones. Other altered sandstones show lower Na_2O contents. Enrichments in CaO and MnO are observed in the yellowish-grey sandstone having a calcite cement. MnO is also high in the

green sandstones. Cu, V, and U enrichments occur in the green sandstones (>10,000 ppm Cu) and in a greenish-grey mudstone sample; two green sandstone samples also show high Ba and Sr (Fig. 15).
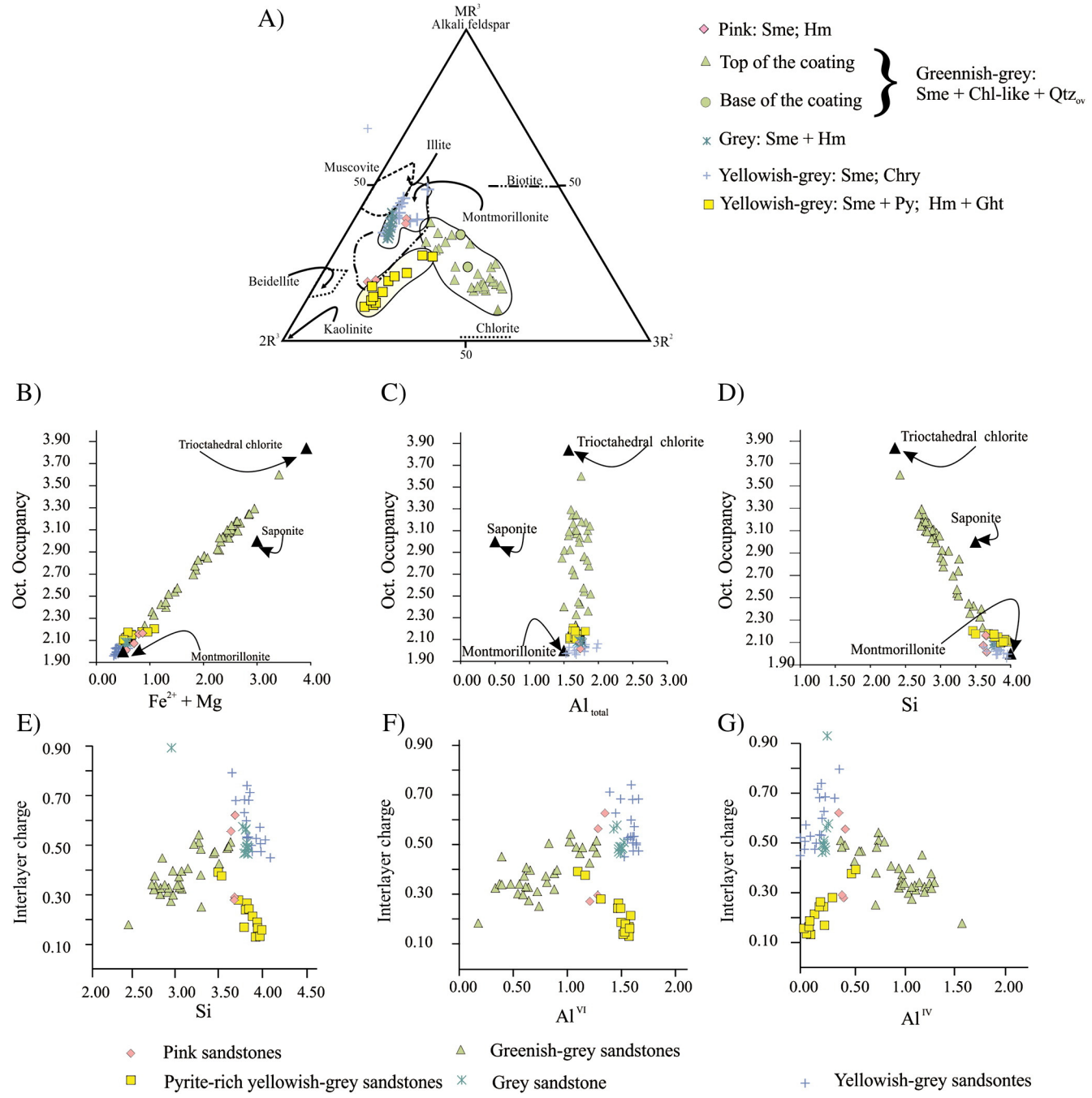
Fig. 13. A–I) Chemical composition of clay minerals (see text for further explanation) of yellowish-grey, pink, grey, greenish-grey rocks, are represented by the coordinates MR^3-$2R^3$-$3R^2$, with silica considered as a excess component, $MR^3 = Na + K + 2Ca$; $2R^3 = (Al + Fe^{3+} - MR^3) / 2$, and $3R^2 = (Mg + Mn + Fe^{2+}) / 3$ (Velde, 1985). D–E) The ideal compositions of montmorillonite ($Si_4Al^{VI}_{1.5}R^{2+}_{0.5}M^+_{0.5}O_{10}(OH)_4$), saponite ($Si_{3.5}Al^{IV}_{0.5}R^{2+}_3M^+_{0.5}O_{10}(OH)_4$), and chlorite ($(Si_3Al^{IV}AL^{VI}R^{2+}_5O_{10}(OH)_8$) are shown for comparison. The chemical compositions of clay minerals Chl: chlorite; Chry: chrysocolla; Ght: goethite; Hm: hematite; Py: pyrite; Sme: smectite. (For interpretation of the references to color in this figure, the reader is referred to the web version of this article.)

5. Discussion

During the deposition of the Neuquén Group, the main trend of the paleosurface drainage was N to NNW (DiGiulio et al., 2012), which is consistent with the paleo-currents obtained for the Huincul Formation. In general, the paleo-fauna and paleo-flora indicate that, during the deposition of this formation, warm weather with a marked seasonal rainfall regime evolved to a more humid climate during deposition of the Cerro Lisandro Formation (Garrido, 2000; Sánchez et al., 2008; Garrido, 2011, and references therein).

The geometry of successions in the middle section of the Huincul Formation, dominated by stacked pebbly to coarse-grained paleo-channel bodies interbedded with minor floodplain deposits, indicate that these sedimentary rocks represent the fill of braided rivers formed by high-discharge processes (Miall, 1996). In the lower and upper section of the Huincul Formation, isolated paleo-channels predominate and grade upward into planar laminated sandstones and laminar and massive mudstones (Fig. 3b), suggesting the prevalence of overflow channel and floodplain deposits (Kraus and Wells, 1999). This organization of facies resulted from a combination of climate cycles (humid-arid; Garrido, 2011 and references therein) and tectonic stages developed in an
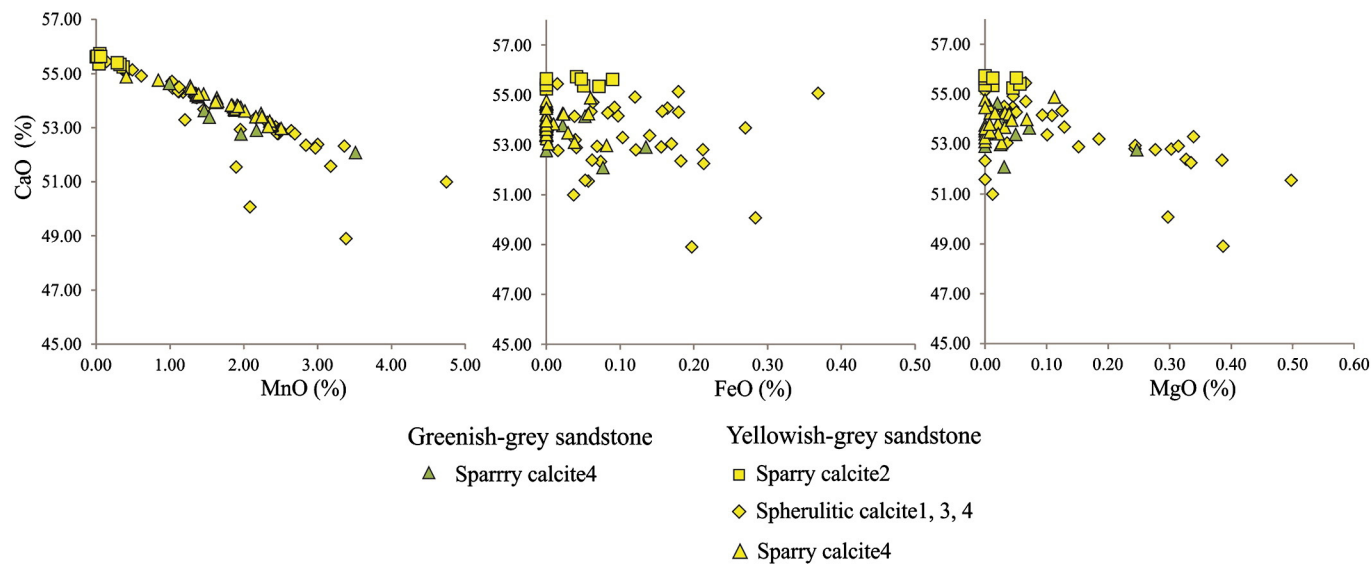
Fig. 14. A–C) Bivariate diagrams showing the chemical composition of various carbonates in yellowish grey and greenish-grey rocks. (For interpretation of the references to color in this figure, the reader is referred to the web version of this article.)

evolving foreland basin related to contractional deformation in the western Andean margin (Maretto and Pángaro, 2005; Silvestro and Zubiri, 2008).

Interconnections among stacked permeable channel strata in the middle section of the Huincul Formation facilitated the migration of several kinds of fluids ranging from early diagenesis to late mineralization stages, resulting in the development of the alteration halos in the sandstones, conglomerates, and mudstones.

5.1. Authigenic minerals formed during early diagenesis

According to the calculated thickness for the overlying rocks (Río Neuquén Subgroup: 370 m; Río Colorado Subgroup: 180 m (Garrido, 2011), Malagrüe Group: 450 m (Rodríguez, 2011), the Huincul Formation in the study area was buried to a depth of ~1000 m. Thus, during sandstone burial the temperature did not exceeded 50 °C, assuming a normal geothermal gradient (25 °C/km; Blatt, 1979; Boggs, 1992). Based on field

Table 3
Microprobe analyses of chrysocolla.

% Peso/point	To 70209-6		To 21107-6								To 21107-17		
	6	7	1	2	2b	3	4	5	9	10	13	14	15
SiO_2	35.93	37.51	39.62	42.10	33.08	43.48	23.66	37.99	40.65	44.34	34.63	41.76	23.49
Al_2O_3	3.08	3.26	3.26	4.07	3.23	4.01	1.84	2.48	2.81	17.16	3.42	4.56	1.91
Fe_2O_3	0.01	0.01	0.03	0.05	0.02	0.08	0.08	0.00	0.03	1.10	0.00	0.05	0.06
MnO	0.00	0.00	0.04	0.01	0.08	0.00	22.68	0.25	0.05	0.01	0.01	0.01	0.01
MgO	0.20	0.12	0.35	0.53	0.32	0.32	0.27	0.19	0.08	1.29	0.08	0.14	0.04
CaO	0.81	0.93	1.23	1.25	1.05	1.11	2.37	0.83	1.10	0.56	1.10	1.21	1.05
Na_2O	0.00	0.00	0.00	0.00	0.00	0.00	0.00	0.03	0.00	0.37	0.00	0.00	0.02
K_2O	0.01	0.00	0.12	0.17	0.04	0.08	0.02	0.03	0.01	2.78	0.01	0.00	0.01
CuO	49.86	47.50	40.94	36.54	38.32	39.28	34.09	32.78	48.58	23.19	49.78	47.41	48.35
Total	89.91	89.33	85.58	84.72	76.16	88.37	85.00	74.58	93.31	90.81	89.03	95.13	74.94
Number of cations for 9 oxygen													
Si	2.07	2.12	2.24	2.29	2.14	2.29	1.62	2.40	2.20	1.76	2.02	2.13	1.79
Ti	0.00	0.00	0.00	0.00	0.00	0.00	0.00	0.00	0.00	0.00	0.00	0.00	0.00
Al	0.42	0.44	0.43	0.52	0.49	0.50	0.30	0.37	0.36	1.60	0.47	0.55	0.34
Fe^{3+}	0.00	0.00	0.00	0.00	0.00	0.01	0.01	0.00	0.00	0.07	0.00	0.00	0.01
Mn^{2+}	0.00	0.00	0.00	0.00	0.00	0.00	1.32	0.01	0.00	0.00	0.00	0.00	0.00
Mg^{2+}	0.02	0.01	0.03	0.04	0.03	0.03	0.03	0.02	0.01	0.08	0.01	0.01	0.00
Ca^{2+}	0.05	0.06	0.07	0.07	0.07	0.06	0.17	0.06	0.06	0.02	0.07	0.07	0.09
Na^+	0.00	0.00	0.00	0.00	0.00	0.00	0.00	0.01	0.00	0.06	0.00	0.00	0.01
K^+	0.00	0.00	0.02	0.02	0.01	0.01	0.00	0.00	0.00	0.28	0.00	0.00	0.00
Cu^{2+}	2.17	2.03	1.75	1.50	1.87	1.56	1.77	1.56	1.99	0.70	2.19	1.83	2.79
Other cations	0.07	0.07	0.13	0.14	0.12	0.11	1.53	0.10	0.08	0.51	0.08	0.08	0.11
O	5.00	5.00	5.00	5.00	5.00	5.00	5.00	5.00	5.00	5.00	5.00	5.00	5.00
Si	2.07	2.12	2.24	2.29	2.14	2.29	1.62	2.40	2.20	1.76	2.02	2.13	1.79
Al^{IV}	0.00	0.00	0.00	0.00	0.00	0.00	0.38	0.00	0.00	0.24	0.00	0.00	0.21
$H_{(2-x)}$	1.58	1.56	1.57	1.48	1.51	1.50	2.00	1.63	1.64	0.64	1.53	1.45	1.86
nH_2O (x < 1)													
Al_x	0.42	0.44	0.43	0.52	0.49	0.50	0.00	0.37	0.36	1.36	0.47	0.55	0.14
$(OH)_4$	4.00	4.00	4.00	4.00	4.00	4.00	4.00	4.00	4.00	4.00	4.00	4.00	4.00
Cu_{2-x}	1.75	1.60	1.31	0.98	1.38	1.07	1.77	1.19	1.63	0.67	1.72	1.28	2.65

Table 4
Microprobe analyses of sulfates.

Sample	To270410-15					To21107-17		To-21107-6	To270410-15		To21107-17					To-21107-6			
Point	5	6	35	17	26	5	6	8	8	25	8	9	16	20	21	11	12	15	21
Type of Sulfate	Brochantite					Brochantite		Brochantite	Barite3		Barite3					Barite3			
Al_2O_3	0.0	0.0	0.0	0.0	0.0	0.0	0.0	0.0	0.0	0.0	0.0	0.0	0.0	0.0	0.0	0.0	0.0	0.0	0.0
SiO_2	0.0	0.0	0.0	0.0	0.0	0.0	0.0	0.0	0.0	0.0	0.0	0.0	0.0	0.0	0.0	0.0	0.0	0.0	0.0
P_2O_5	0.0	0.0	0.0	0.0	0.0	0.0	0.0	0.0	0.0	0.0	0.0	0.0	0.0	0.0	0.0	0.0	0.0	0.0	0.0
SO_3	18.1	18.3	20.2	18.0	19.4	19.6	17.1	18.0	18.4	25.3	23.3	20.6	29.9	24.7	24.9	25.1	28.6	22.4	19.5
K_2O	0.0	0.0	0.0	0.0	0.0	0.0	0.0	0.0	0.0	0.0	0.0	0.0	0.0	0.0	0.0	0.0	0.0	0.0	0.0
CaO	0.1	0.0	0.1	0.0	0.3	0.1	0.1	0.0	0.7	0.2	0.2	0.4	0.4	0.3	0.3	0.2	0.2	0.4	0.6
V_2O_3	0.0	0.0	0.0	0.0	0.0	0.0	0.0	0.0	0.0	0.0	0.0	0.0	0.0	0.0	0.0	0.0	0.0	0.0	0.0
CuO	70.1	69.0	71.5	70.3	62.1	71.1	62.9	69.6	17.6	9.2	26.0	24.2	6.8	14.8	14.5	11.0	6.5	14.8	24.0
SrO	0.1	0.1	0.1	0.1	1.1	0.0	0.1	0.0	2.1	1.6	0.9	0.6	1.6	1.0	0.9	2.6	1.6	3.4	1.8
BaO	0.2	0.0	0.8	0.3	6.1	0.4	4.6	0.1	34.3	47.1	37.8	36.5	56.1	48.6	45.9	49.2	53.8	39.9	31.9
PbO	0.0	0.0	0.0	0.0	0.0	0.0	0.0	0.0	0.0	0.0	0.0	0.0	0.0	0.0	0.0	0.0	0.0	0.0	0.0
UO_2	0.0	0.0	0.0	0.0	0.0	0.0	0.0	0.0	0.0	0.0	0.0	0.0	0.0	0.0	0.0	0.0	0.0	0.0	0.0
Total	88.54	87.54	92.65	88.72	89.09	91.26	84.76	87.70	73.17	83.31	88.24	82.26	94.74	89.38	86.50	88.02	90.67	80.90	77.91
Cations in base of 4 oxygens																			
Al	0.00	0.00	0.00	0.00	0.00	0.00	0.00	0.00	0.00	0.00	0.00	0.00	0.00	0.00	0.00	0.00	0.00	0.00	0.00
Si	0.00	0.00	0.00	0.00	0.00	0.00	0.00	0.00	0.00	0.00	0.00	0.00	0.00	0.00	0.00	0.00	0.00	0.00	0.00
P	0.00	0.00	0.00	0.00	0.00	0.00	0.00	0.00	0.00	0.00	0.00	0.00	0.00	0.00	0.00	0.00	0.00	0.00	0.00
S	0.58	0.59	0.61	0.58	0.62	0.60	0.58	0.58	0.79	0.91	0.80	0.78	0.94	0.86	0.87	0.88	0.94	0.84	0.77
K	0.00	0.00	0.00	0.00	0.00	0.00	0.00	0.00	0.00	0.00	0.00	0.00	0.00	0.00	0.00	0.00	0.00	0.00	0.00
Ca	0.00	0.00	0.00	0.00	0.01	0.00	0.01	0.00	0.04	0.01	0.01	0.02	0.02	0.02	0.01	0.01	0.01	0.02	0.03
V	0.00	0.00	0.00	0.00	0.00	0.00	0.00	0.00	0.00	0.00	0.00	0.00	0.00	0.00	0.00	0.00	0.00	0.00	0.00
Cu	2.26	2.23	2.16	2.26	2.00	2.19	2.16	2.26	0.76	0.33	0.90	0.92	0.21	0.52	0.51	0.39	0.22	0.56	0.95
Sr	0.00	0.00	0.00	0.00	0.03	0.00	0.00	0.00	0.07	0.04	0.02	0.02	0.04	0.03	0.03	0.07	0.04	0.10	0.05
Ba	0.00	0.00	0.01	0.00	0.10	0.01	0.08	0.00	0.77	0.88	0.68	0.72	0.92	0.88	0.84	0.90	0.92	0.79	0.66
Pb	0.00	0.00	0.00	0.00	0.00	0.00	0.00	0.00	0.00	0.00	0.00	0.00	0.00	0.00	0.00	0.00	0.00	0.00	0.00
U	0.00	0.00	0.00	0.00	0.00	0.00	0.00	0.00	0.00	0.00	0.00	0.00	0.00	0.00	0.00	0.00	0.00	0.00	0.00

observations and petrographic analyses (which reveal deformed micas, lithic clasts, and fractured quartz and feldspar grains), the sediments of the Huincul Formation were mechanically compacted. The presence of irregularly distributed kaolinite with vermicular and book-like habits (Ketzer et al., 2003) in the sandstones and mudstones (Fig. 7A) suggests its formation during eogenesis under humid conditions, by the interaction of low-pH groundwater with detrital aluminosilicate minerals (Emery et al., 1990). Spherulitic calcite1 in mudstones and sandstones along with bioturbations, suggest that calcite1 precipitated in the vadose zone (Klappa, 1978; Calvet et al., 1991; Kosir, 2004). The continuous layer of this calcite at the top of mudstones indicates the development of a paleo-aridisoil (Worden and Morad, 2003). Multi-episodic downward clay infiltrations occurred below the mudstones, in the unconfined meandering paleo-channel deposits, resulting in thick clay coatings (Worden and Morad, 2003) in the greenish-grey sandstones (Figs. 4, 9A-C). Progressive burial and introduction of oxygenated meteoric water caused the reddening of the Huincul Formation by the precipitation of hematite after the breakdown of ferrous iron bearing oxides and silicates (Fig. 16; Walker, 1976; Brown, 1984; Walker, 1989). This hematite coating has been preserved in the reddish brown mudstones of the study area (Fig. 17). In other sediment-hosted copper deposits from the Neuquén Basin, some sandstones layers from the Huincul Formation have preserved hematite coating (Rainoldi et al., 2014).

The partial dissolution of feldspar and volcanic lithic clasts liberated traces of Ba that, along with the sulfate available from the Huincul Formation waters (23–28 mg/l; Sosic, 1978), caused the local precipitation of the early barite rim cement (Fig. 7C). Subsequent compaction and circulation of formation waters enriched in Si and Ca may have favored the precipitation of quartz replacing the cellular texture of fossil roots and logs and calcite1cement. The unusual presence of illite-smectite mixed layers R1 (Figs. 6A, 16) in this shallower environment (~1 km buried) suggests that these minerals were incorporated in the fine-grained detritus (i.e., as inherited clay minerals).

Tubes and clusters of concretions formed by poikilotopic calcite2 with red luminescence are similar to calcite pipes described in the Candeleros and Huincul Formations at El Porvenir area (Rainoldi et al., 2015) and in other reservoir rocks associated with faults (e.g., Entrada Sandstone, Utah; Garden et al., 2001). These concretions indicate a change in partial pressure of CH_4 and/or CO_2 rather than signaling fluid mixing. During upward hydrocarbon migration, reaction with rocks produced organic acids that evolved to CO_2 or CH_4. When these fluids moved through fractures, the partial pressure of exsolved CH_4 and/or CO_2 would decline and result in local calcite precipitation (see also Garden et al., 2001). The red luminescence of this calcite is consistent with its MnO content (0.01–0.28%; Fig. 14) and its precipitation in a reduced environment. Thus, these pipes are interpreted as the product of the first reduced fluids (CH_4-CO_2) to have circulated through the Huincul Formation, before the arrival of liquid hydrocarbons (Fig. 16).

5.2. Alteration of redbeds by liquid hydrocarbons

During the Andean orogeny, reactivations of previous Triassic and Jurassic structures at the Huincul High (Maretto and Pángaro, 2005) triggered subsurface fluid seepage (formation water + hydrocarbons), breaking seals (Vaca Muerta Formation), and producing the up-flow of oil and formation water from the Lotena, Mulichinco, and Centenario reservoir rocks (Cabaleiro et al., 2002; Montagna et al., 2010) to the Neuquén Group. Evidence of this process is the conspicuous bitumen impregnations in the most permeable strata of the Neuquén Group described in the study area, in the Los Chihuidos High (e.g., Sapo Sur and Grillo Cu deposits, Rainoldi et al., 2014), and in other regions of the Huincul High (e.g., Barda González, La Cuprosa, and El Porvenir SHC deposits; Giusiano et al., 2006, 2008; Pons et al., 2009; Paz et al., 2014; Rainoldi et al., 2015). Additional evidence for oil emplacement in the Huincul Formation at Tordillos is found in the numerous organic-rich fluid inclusions hosted in the micro-quartz overgrowths, calcite3, 4, and barite2 cements (see also Pons et al., 2015a). The chronology and chemical changes of the various cements observed in the Huincul Formation document a complex history of multiple fluids (hydrocarbons,

Sample	To70209-6								To270410-15					To270410-15			
Point	1	4	5	8	12	13	21	24	31	33	34	7	9	18	19	21	10
Type of Sulfate	Barite2				Barite2				Barite2					Barite1			
Al_2O_3	0.0	0.0	0.0	0.0	0.0	0.0	0.0	0.0	0.0	0.0	0.0	0.0	0.0	3.9	11.2	2.5	0.0
SiO_2	0.0	0.0	0.0	0.0	0.0	0.0	0.0	0.0	0.0	0.0	0.0	0.0	0.0	7.5	17.2	4.3	0.0
P_2O_5	0.0	0.0	0.0	0.0	0.0	0.0	0.0	0.0	0.0	0.0	0.0	0.0	0.0	0.1	0.1	0.1	0.0
SO_3	16.7	32.5	33.4	33.4	19.1	24.3	33.2	31.3	33.4	20.1	22.9	33.0	32.1	24.5	21.2	31.2	29.0
K_2O	0.0	0.0	0.0	0.0	0.0	0.0	0.0	0.0	0.0	0.0	0.0	0.0	0.0	0.0	0.0	0.0	0.0
CaO	0.8	0.2	0.1	0.6	0.3	0.1	0.8	0.2	0.2	0.2	0.2	0.5	0.0	0.0	0.0	0.0	0.3
V_2O_3	0.0	0.0	0.0	0.0	0.0	0.0	0.0	0.0	0.0	0.0	0.0	0.0	0.0	0.0	0.0	0.0	0.0
CuO	7.3	0.0	0.1	0.5	0.5	2.9	2.2	2.1	0.0	0.4	0.1	0.2	0.8	0.0	9.4	3.0	1.6
SrO	0.0	0.0	0.0	0.0	0.0	0.0	0.0	0.0	4.4	3.5	3.1	1.5	0.8	0.0	0.0	0.0	0.0
BaO	43.9	63.7	65.3	63.6	57.8	54.1	63.8	62.0	60.5	57.7	62.0	65.4	64.2	47.7	41.8	60.7	61.3
PbO	0.0	0.0	0.0	0.0	0.0	0.0	0.0	0.0	0.0	0.0	0.0	0.0	0.0	0.1	0.0	0.1	0.0
UO_2	0.0	0.0	0.0	0.0	0.0	0.0	0.0	0.0	0.0	0.0	0.0	0.0	0.0	0.0	0.0	0.0	0.0
Total	68.67	96.39	98.96	98.09	77.71	81.34	99.96	95.64	98.48	81.95	88.22	100.62	97.84	83.82	100.87	101.93	92.08
Cations in base of 4 oxygens																	
Al	0.00	0.00	0.00	0.00	0.00	0.00	0.00	0.00	0.00	0.00	0.00	0.00	0.00	0.19	0.42	0.11	0.00
Si	0.00	0.00	0.00	0.00	0.00	0.00	0.00	0.00	0.00	0.00	0.00	0.00	0.00	0.31	0.55	0.16	0.00
P	0.00	0.00	0.00	0.00	0.00	0.00	0.00	0.00	0.00	0.00	0.00	0.00	0.00	0.00	0.00	0.00	0.00
S	0.82	0.99	0.99	0.99	0.86	0.93	0.97	0.97	0.99	0.86	0.88	0.98	0.98	0.77	0.51	0.85	0.96
K	0.00	0.00	0.00	0.00	0.00	0.00	0.00	0.00	0.00	0.00	0.00	0.00	0.00	0.00	0.00	0.00	0.00
Ca	0.05	0.01	0.00	0.03	0.02	0.00	0.03	0.01	0.01	0.01	0.01	0.02	0.00	0.00	0.00	0.00	0.01
V	0.00	0.00	0.00	0.00	0.00	0.00	0.00	0.00	0.00	0.00	0.00	0.00	0.00	0.00	0.00	0.00	0.00
Cu	0.36	0.00	0.00	0.01	0.02	0.11	0.06	0.07	0.00	0.02	0.00	0.00	0.02	0.00	0.23	0.08	0.05
Sr	0.00	0.00	0.00	0.00	0.00	0.00	0.00	0.00	0.10	0.12	0.09	0.04	0.02	0.00	0.00	0.00	0.00
Ba	1.13	1.02	1.01	0.98	1.37	1.08	0.98	1.01	0.93	1.28	1.25	1.01	1.02	0.78	0.52	0.87	1.06
Pb	0.00	0.00	0.00	0.00	0.00	0.00	0.00	0.00	0.00	0.00	0.00	0.00	0.00	0.00	0.00	0.00	0.00
U	0.00	0.00	0.00	0.00	0.00	0.00	0.00	0.00	0.00	0.00	0.00	0.00	0.00	0.00	0.00	0.00	0.00

barium-rich brines, and copper-rich brines) and their possible mixing with interstitial waters of the Huincul Formation.

The incoming of hydrocarbons and brine into the redbed produced: 1) an increase in temperature (i.e., the temperature of reservoir waters in the oilfield was 80 to 100 °C, Pons et al., 2015b), and 2) the oxidation of hydrocarbons and the generation of organic acids which controlled the alkalinity and the P_{CO2} of the system (Willey et al., 1975; Carothers and Kharaka, 1978). Fluctuations in the pH and P_{CO2} in the fluids are reflected in multiple stages of dissolution of early cements and precipitation of new generations of calcite (calcite3 and 4; Fig. 16) (James and Choquette, 1990). Hematite dissolution and reduction of Fe^{3+} to Fe^{2+} resulted in sandstone discoloration (Fig. 16). Dysfunctional carboxylic acids may have promoted the dissolution of aluminosilicate grains (Surdam et al., 1989) and the released Al could have been complexed with these organic acids and thus became available for transport (MacGowan and Surdam, 1988) until their destabilization due to Eh conditions to re-deposit Al as clay minerals (Rainoldi et al., 2014; smectite, chlorite-corrensite mixed layers, and/or chlorite; Fig. 16).

In the thickest and most permeable paleo-channels of the Huincul Formation (middle section; Fig. 3B), bitumen impregnations are more abundant along with meso-quartz overgrowths, smectite, multistage calcite(3, 4), and pyrite. Meso-quartz overgrowth precipitated in this zone did not have significant clay coatings, suggesting that the grain-rimming clays prevented the precipitation of quartz overgrowth (cf. Hornibrook and Longstaffe, 1996; Baker, 1991; Worden and Morad, 2003; Anjos et al., 2003; Billault et al., 2003; Ketzer et al., 2003; Ajdukiewicz and Larese, 2012). The silica source for quartz overgrowth precipitation may have been the dissolution of detrital clasts caused by hydrocarbons reactions and dissolved silica from the warm water that migrated with hydrocarbon (Bjørlykke and Egeberg, 1993). In the yellowish-grey sandstones with abundant pyrite, the deviation of clay mineral compositions into the typical montmorillonite field (Fig. 13A) could be caused by iron oxide impurities derived from the supergene alteration of pyrite that also caused the leaching of interlayer cations (Fig.

13F). Dissolution of early cements and detrital clasts increased the porosity of sandstones up to 24% of total volume (Table 1; Fig. 16), where calcite cement is absent. This dissolution is also observed in the depletion of Al_2O_3, Fe_2O_3total, and MgO with respect to the reddish brown rocks (Fig. 15). The precipitation of the sparry calcite4 at the contact between bitumen and calcite2, along with its organic fluid and pyrite inclusions, suggest its formation from the reaction of calcite2 with hydrocarbons. The MnO enrichment of calcite3 and 4 suggests their precipitation under reduced conditions. Samples with high Ba content (Fig. 15, Table B.3) located west of the main paleo-channel zones (Fig. 3A) are cemented by coarse barite2 crystals that host abundant primary organic fluid inclusions (Pons et al., 2015a), suggesting precipitation in contact with hydrocarbon fluids (Fig. 17). This zone of high Ba may have been close to subsurface feeder conduits (e.g., faults; Fig. 17), through which hydrocarbons migrated with chloride-rich formation waters (Montagna et al., 2010) with temperatures >80 °C (Pons et al., 2015b). Barium could be transported as a chloride complex under reduced conditions and precipitated when reduced formation waters were oxidized (Cooke et al., 2000) and cooled (Blount, 1977) by mixing with interstitial water of the Huincul Formation.

Chlorite and chlorite-corrensite mixed layers were formed after montmorillonite in the greenish-grey sandstones. Additions of Mg^{2+} and Fe^{2+} are required to form chlorite and corrensite-chlorite mixed layers from the dissolution products of montmorillonite, and they could be provided by the dissolution of detrital mafic minerals (Fig. 3B) and/or formation waters that migrated with hydrocarbons (Pons et al., 2014). The persistence of minor amount of montmorillonite and the mixing of chlorite-corrensite mixed layers with chlorite mean that the chloritization process did not reach completion. The most probable reaction could be dissolution of montmorillonite and crystallization of early corrensite (Beaufort et al., 2015, and references therein) at temperatures lower than 100 °C (Morrison and Parry, 1986; Hillier, 1993; Worden and Morad, 2003; Hillier et al., 2006) and then, progressive transformation of corrensite to chlorite through a dissolution crystallization mechanism (Beaufort et al., 1997; Murakami et al., 1999) with

Table 5
Iron oxide semiquantitative compositions.

Sample	To 111209-16 grey					To 21107-12[a] yellowish-grey		
Point	15	14	13	12	11	21	22	23
O	50.51	50.44	51.78	50.66	50.46	26.00	33.30	29.70
Na	1.02	0.08	0.45	0.10	0.10	0.00	0.00	0.00
Mg	0.54	0.07	0.39	0.01	0.05	0.00	1.30	0.50
Al	0.99	0.46	1.23	0.46	0.41	1.59	5.20	2.90
Si	2.04	0.85	2.38	0.91	0.94	3.54	8.00	4.10
S	0.12	0.01	0.02	0.06	0.03	0.00	0.10	0.00
K	0.00	0.04	0.10	0.04	0.07	0.00	0.30	0.20
Ca	0.10	0.08	0.13	0.05	0.07	0.49	1.90	1.50
Ti	0.67	2.25	1.45	1.93	2.20	0.62	0.50	0.60
Mn	0.61	0.16	0.36	0.14	0.20	0.00	8.50	7.80
Fe	41.48	43.15	41.07	43.82	43.08	66.90	36.80	48.80
Cu	0.00	0.03	0.00	0.12	0.03	0.00	3.10	2.70
V	1.92	2.38	0.66	1.69	2.36	1.25	0.80	0.90
Cl	0.00	0.00	0.00	0.00	0.00	0.00	0.50	0.30

[a] LamaRX laboratories Universidad Nacional de Córdoba.

increasing temperature and or reaction time (Worden and Morad, 2003; and references therein). Dissolution crystallization is particularly efficient for chloritization processes that operate in fluid-dominated systems (open systems with high fluid-rock ratios; Beaufort et al., 2015 and references therein). Such conditions prevailed in the isolated permeable layers of the lower section of the Huincul Formation (Fig. 3B) that yielded a focused flow pathway (Fig. 17).

The partial transformation of montmorillonite into chlorite-corrensite mixed layers and chlorite produced an additional source of silica, resulting in the precipitation of micro-quartz overgrowth (Mosser-Ruck et al., 2010) probably at temperatures above 100 °C (Robinson and Santana de Zamora, 1999); homogenization temperatures between 90 and 120 °C were obtained in aqueous fluid inclusions hosted in calcite4, barite2, and quartz overgrowth (Pons et al., 2015a). Interstitial Mn-rich calcite with inclusions of pyrite and bitumen in these sandstones is indicative of reducing conditions.

The grey sandstones contain abundant montmorillonite with traces of secondary V-bearing specular hematite. Vanadium could have been carried as V^{3+} by the incoming of reduced fluids complexed with dissolved organic matter (Granger, oral communication, 1983 in Goldhaber et al., 1990). The occurrence of vanadium in petroleum-related fluids has been observed previously in bitumen from the Vaca Muerta Formation (Parnell and Carey, 1995) and worldwide in oil fields in bitumen and asphalt deposits (DeGolyer, 1924 and references therein; Breit and Wanty, 1991; Parnell and Carey, 1995). The presence of specular hematite in grey sandstone in this shallow environment (<1 km) suggests temperatures of formation >100 °C (Sugimoto et al., 1996; Catling and Moore, 2003).

The location of the grey and greenish-grey sandstones between the reddish-brown and yellowish-grey sandstones and conglomerates (Fig. 17) suggests their formation by specific geochemical conditions. For example, the presence of montmorillonite and specular hematite in the grey sandstones and chlorite, corrensite-chlorite mixed layer, smectite, and traces of pyrite in the greenish-grey sandstones, are indicative of variable redox conditions. Decreasing amounts of sulfides and crystallization of Fe^{2+} bearing phyllosilicates of the chlorite group (at the expense of smectite) and secondary hematite with smectite indicate a decrease in sulfur fugacity of the solution toward the outer part of the reduced zone. Thus, the grey and greenish-grey rocks represent more oxidizing and reducing conditions, respectively, at a redox front (Rainoldi et al., 2014) and lower sulfur fugacity. The MgO and Fe_2O_{3total} enrichment exhibited by the greenish-grey rocks (Fig. 15) is coincident with the presence of a thick clay coating of montmorillonite and chlorite-corrensite mixed layers and chlorite. This enrichment is higher than in the grey rocks which contain a thin clay coating of only montmorillonite (Fig. 15). The redox front in Tordillos deposit differs from the regional scale redox front located in Los Chihuidos High (Rainoldi et al., 2014) in that the former is local due the lenticular morphology of the preserved reddish-brown mudstones and claystones interbedded with the paleo-channels of the Huincul Formation (Fig. 17) whereas the latter is continuous at regional scale.

5.3. Cu-mineralization

Copper mineralization is hosted in green sandstones and conglomerates within-altered rocks, and its spatial association with bitumen at macro- and micro-scale indicates that copper-rich fluids entered into the altered paleo-channel of the Huincul Formation when it was reduced and acting as an oil reservoir or carrier bed (e. g. replacement textures of barite1 and barite2 by chalcocite group and iron-copper sulfides in contact with bitumen; Fig. 10). The local feeder zones for these hydrocarbon-bearing fluids seem to have been the vertical tubes with hydrocarbons exposed west of the main paleo-channels zone (Fig. 3A). These tubes are now filled with copper mineralization and bitumen. In consequence, hydrocarbons induced reduction and lead to iron-copper and copper-sulfides deposition. The presence of bornite and chalcopyrite as an assemblage imply temperatures of formation above 100 °C (Haynes and Bloom, 1987). The predominance of sulfides from the chalcocite group suggests that fluids had low sulfidation state (Einaudi et al., 2003). Barite and pyrite were the local source of sulfur. The dissolution and replacement of barite1, 2 must have occurred by reacting with warm chloride brines (~100 °C) chlorides carrying copper (Blount, 1977) and a decrease in temperatures produce the precipitation of barite3.

Formation waters from the main reservoirs rocks in the study area (Lotena and Mulichinco formations; Fig. 2A) have salinities range between 36 to 160 g/l NaCl eq. (Vottero and González, 2002, Malone et al., 2002) and temperatures varies from 72 to 100 °C (1900 to 3000 m depths). These brines could have leached copper from underlying basement rock and redbeds strata of Tordillos Formation, Rayoso Group, and Neuquén Group (Fig. 2A). At Paradox Basin, for similar deposits Hahn and Thorson (2006) described the convection of warm (70–110 °C) brines (50–200 g/l NaCl eq.) as the main fluids capable to leach copper from the redbeds and transport it in the form of chlorides complex (Brown, 1971, Rose, 1976, Brown, 2005).

Organic acids generated during the oxidation of hydrocarbons by mineralizing fluids may have induced the dissolution of silicates and cements (Blake and Walter, 1999), explaining the absence of clay minerals and carbonate cements in the green rocks, and the depletion of major oxides in the green sandstones, including SiO_2 (Fig. 15). Zones of anomalous feldspar destruction and copper sulfide replacing previous carbonate cement were observed in the Zambian Copperbelt (Darnley, 1960). Acid also is produced by oxidation of pre-existing pyrite and replacement with later copper-rich sulfides (Hitzman et al., 2005).

The replacement of pyrite by Cu sulfides re-mobilized Fe^{+2} (Fig. 17; Brown, 1984) that could have been precipitated as additional pyrite (Sverjensky, 1987; Figs. 16, 17) in the altered sandstones in contact with the green sandstones, increasing the iron content in these samples (Fig. 15).

5.4. Supergene alteration stage

The Andean compression produced the folding and uplift of the Neuquén Group (Leanza et al., 2005) which favored the incoming of oxidized meteoric water that generated the supergene alteration of copper sulfides to form copper sulfates, carbonates, silicates, barium, potassium and copper urovanadates, and iron-copper oxides (Fig. 17). The presence of brochantite in contact with Cu sulfides and cuprite in contact with bitumen points to a decrease of oxygen fugacity (Fig. 11). Higher brochantite content than malachite and cuprite indicates that the
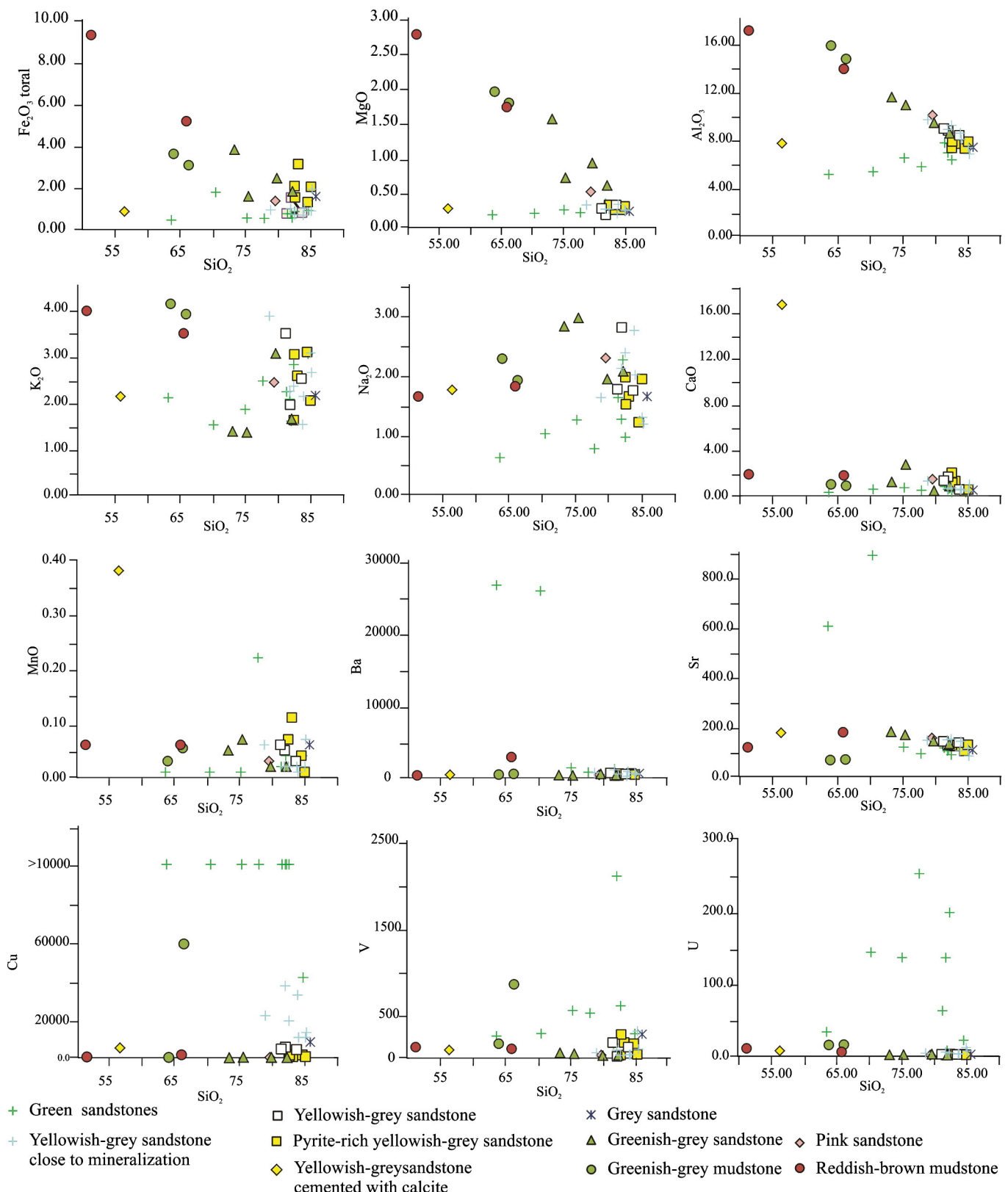
Fig. 15. A) Harker-type diagrams for major and minor elements in the unaltered (brownish-red mudstones), altered (yellowish grey, grey, and greenish-grey sandstones), and mineralized (green sandstones). (For interpretation of the references to color in this figure, the reader is referred to the web version of this article.)

oxidation of sulfides occurred under slightly acidic conditions (pH 5–6; Sillitoe, 2005). Textures of supergene minerals reveal that the urovanadates formed after brochantite. Hence, the decrease of the sulfate concentration in the aqueous solutions after brochantite formation,

may have also decreased the solubility of uranyl cation (Langmuir, 1978), favoring the precipitation of urovanadates (Fig. 11).

The surface and subsurface geochemical data (Fig. 15; Pons et al., 2014) indicates that higher concentrations of uranium in the Huincul
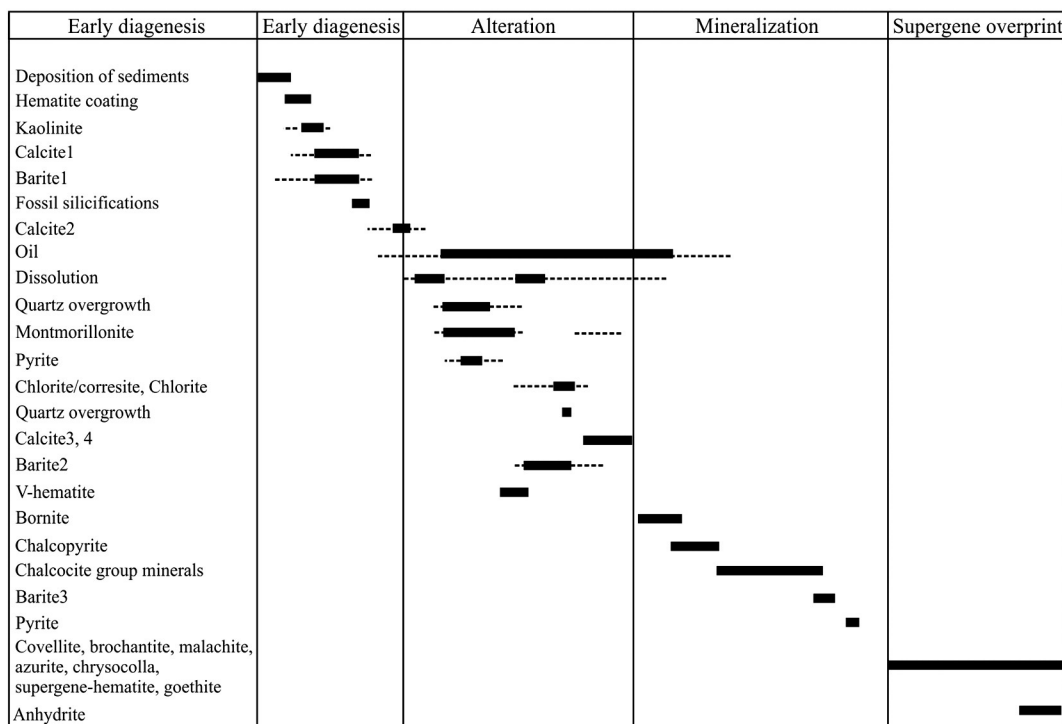
Fig. 16. Paragenetic sequence of diagenetic, alteration and copper minerals.

Formation occur in areas with abundant bitumen impregnations, high concentrations of copper and vanadium, and supergene minerals with uranium and copper. Uranium and vanadium could have been leached from the bitumen to re-precipitate as potassium, barium and copper urovanadates during the supergene stage (Pons et al., 2014).

Surrounding the zones with supergene copper minerals are halos of sandstones and conglomerate cemented by supergene iron oxides and

hydroxides after pyrite. Hematite coatings on dioctahedral smectite in the pink sandstones could have resulted from the supergene alteration of microcrystal of pyrite. Similar alteration halos occur southeast of the study area, in La Cuprosa deposit hosted in the Portezuelo Formation of the Neuquén Group (Paz, 2015). Relict smectite coatings in the yellowish-grey sandstones have traces of copper that could have been added into the interlayer sites during the supergene alteration of copper
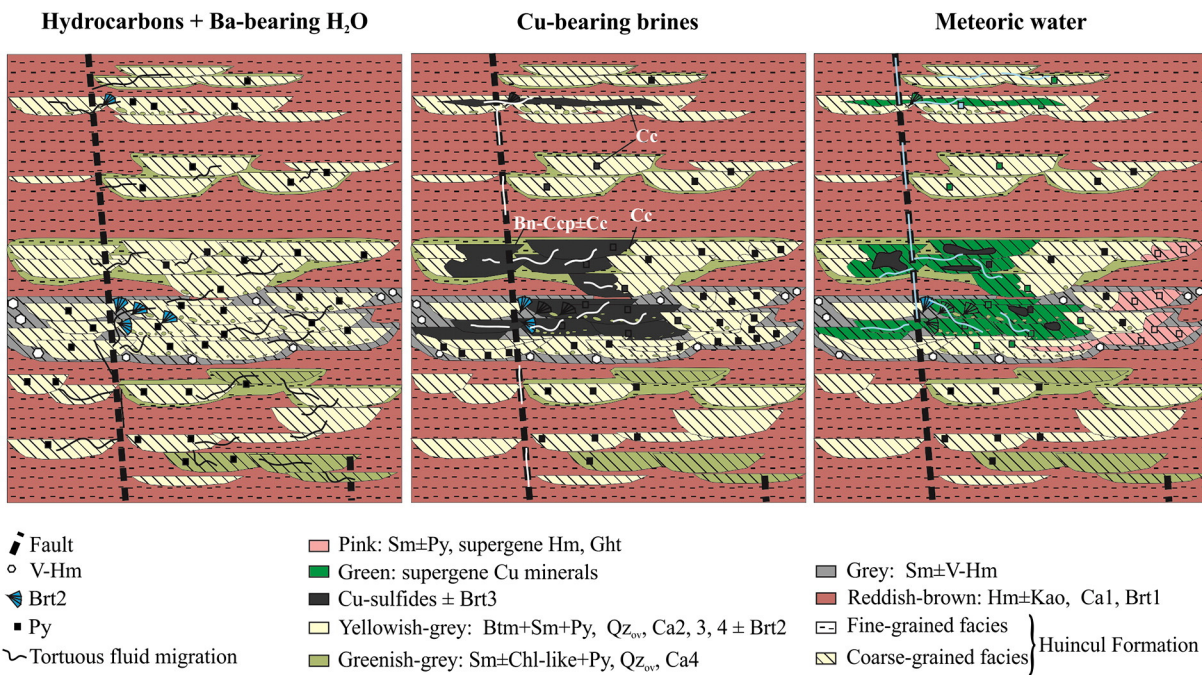
Fig. 17. Schematic model of fluid migrations in the Huincul Formation during the warm A) hydrocarbons-bearing fluids, B) Cu-bearing brines, and C) late meteoric water circulations. Bn: bornite; Btm: bitumen; Btr1, 2, 3: barite1, 2, 3; Ca1,2, 3, 4: calcite1, 2, 3, 4; Ccp: chalcopyrite; Cc: chalcocite group minerals; Chl: chlorite; Ght: goethite; Hm: hematite; Kao: kaolinite; Py: pyrite; Qz$_{ov}$: quartz overgrowth; Sme: smectite.

sulfides. Consequently, the composition of smectite reflects the transition from Cu-rich smectite to chrysocolla (Table 3).

6. Concluding remarks

This study presents a detailed description of the alteration halos and the least-altered sedimentary rocks of a stratiform-copper deposit located in the Neuquén Basin of Argentina. Over 21 recorded sediment-hosted copper deposits are known in this basin, they typically are located above major structures of the Neuquén basin, and have regional alteration of host rocks around mineralized copper strata with bitumen impregnations. These characteristics can be a useful guide to explore for similar deposits in poorly explored regions of the basin and similar basins worldwide. The early digenetic minerals (pore filling kaolinite and calcite layer in mudstone) of the Huincul Formation point to a marked seasonal rainfall regime during early diagenesis. The progressive burial (~1000 m depth and temperatures ~50 °C) produced mechanical compaction followed by infiltration of meteoric water that caused breakdown of ferrous iron bearing minerals and silicates, which in turn caused reddening of the rocks.

During the Andean orogeny, reactivation of previous Triassic and Jurassic structures in the Huincul High triggered subsurface fluid seepage, breaking seals and producing several pulses and up-flows of: 1) oil and formation water from reservoir rocks, 2) warm basin brines and 3) late down flow of meteoric water into the Neuquén Group.

At Tordillos, alteration was produced by the interaction of reducing hydrocarbons with authigenic minerals in the red sandstones and conglomerates, generating an increase in porosity due to the partial dissolution of clasts and early cements. Montmorillonite replaced early Al-bearing minerals such as kaolinite or inherited phyllosilicates and K-feldspar, and hematite was dissolved, to precipitate iron as pyrite in the altered sedimentary rocks. Mixtures of chlorite and chlorite-corrensite replaced montmorillonite at the redox front between yellowish-grey and unaltered reddish brown mudstones which have preserved authigenic minerals from early diagenesis. The oxidation of hydrocarbons locally produced Mn- rich calcite2, 3, and 4 which occluded the porosity.The resulting yellowish-grey, greenish-grey, and grey alteration halos may help in the search for local feeder zones of reduced fluids (hydrocarbons) ± formation waters. The incoming brines capable of metal transport used the same conduits as previous fluids, and these conduits are consistently located in the coarsest-grained facies of the altered halos (yellowish-grey sandstones and conglomerates). Late meteoric water infiltration caused the supergene alteration minerals that also could be used as exploration guides with brochantite, malachite, and cuprite close to the hypogene copper sulfides and chrysocolla, copper bearing smectite and iron oxides with manganese and traces of vanadium and copper as external halos of the mineralized zones.

Supplementary data to this article can be found online at http://dx.doi.org/10.1016/j.oregeorev.2016.06.011.
.

Acknowledgements

References

Ajdukiewicz, J.M., Larese, R.E., 2012. How clay grain coats inhibit quartz cement and preserve porosity in deeply buried sandstones: observations and experiments. Am. Assoc. Pet. Geol. Bull. 96, 2091–2119.

Anjos, S.M.C., De Ros, L.F., Silva, C.M.A., 2003. Chlorite authigenesis and porosity preservation in the Upper Cretaceous marine sandstones of the Santos Basin, offshore eastern Brazil. In: Worden, R.H., Morad, S. (Eds.), Clay Minerals Cements in Sandstones. 34 Special Publication International Association of Sedimentologists, Oxford, pp. 291–316.

Baker, J.C., 1991. Diagenesis and reservoir quality of the Aldebaran Sandstone, Denison Trough, east-central Queensland, Australia, in Burley, S.D. In: Worden, R.H. (Ed.)-Sandstone Diagenesis: Recent and Ancient. International Association of Sedimentologists Reprint Series vol. 4. Wiley-Blackwell, pp. 563–582.

Beaufort, D., Baronnet, A., Lanson, B., Meunier, A., 1997. Corrensite: a single phase or a mixed-layer phyllosilicate in the saponite-to-chlorite conversion series? A case study of Sancerre-Couy deep drill hole (France). Am. Mineral. 82, 109–124.

Beaufort, D., Rigault, C., Billon, S., Billault, V., Inoue, A., Inoue, S., Patrier, P., 2015. Chlorite and chloritization processes through mixed-layer mineral series in low-temperature geological systems - a review. Clay Miner. 50, 497–523.

Billault, V., Beaufort, D., Baronnet, A., Lacharpagne, J.C., 2003. A nanopetrographic and textural study of grain coating chlorites in sandstone reservoirs. Clay Miner. 38, 315–328.

Bjørlykke, K., Egeberg, P.K., 1993. Quartz cementation in sedimentary basins. Am. Assoc. Pet. Geol. Bull. 77, 1538–1548.

Blatt, H., 1979. Diagenetic processes in sandstones. In: Scholle, P., Schulger, P. (Eds.), Aspects of diagenesis. Society of Economic Paleontologists and Mineralogists, Special Publication 26, pp. 141–157.

Blount, C.W., 1977. Barite solubility and thermodynamic up to 300 °C and 1400 bars. Am. Mineral. 62, 942–957.

Boggs Jr., S., 1992. Petrology of sedimentary rocks. Maxwelll Macmillan International, New York (707 p.).

Breit, G.N., Wanty, R.B., 1991. Vanadium accumulation in carbonaceous rocks: a review of geochemical controls during deposition and diagenesis. Chem. Geol. 91, 83–97.

Blake, R.E., Walter, L.M., 1999. Kinetics of feldspar and quartz dissolution at 70–80 °C and near-neutral pH: effects of organic acids and NaCl. Geochim. Cosmochim. Acta 63, 2043–2059.

Brown, A.C., 1971. Zoning in the White Pine copper deposit, Ontonagon County, Michigan. Econ. Geol. 66, 543–573.

Brown, A.C., 1984. Alternative source of metals for stratiform copper deposits. Precambrian Res. 25, 61–74.

Brown, A.C., 2005. Refinements for footwall redbed diagenesis in the sediment-hosted stratiform copper deposits model. Econ. Geol. 100, 765–771.

Cabaleiro, A., Cazau, L., Lasalle, D., Penna, E., Robles, D., 2002. Los Reservorios de la Formación Centenario. Rocas Reservorios de las Cuencas Productivas de la Argentina. In 5°Congreso de Exploración y Desarrollo de Hidrocarburos. Proceedings, pp. 407–414.

Calvet, F., Wright, V.P., Giménez, J., 1991. Microcodium: descripción y origen. Implicaciones paleogeográficas y paleogeomorfológicas. In Grupo Español del Terciario, Comunicaciones I Congreso, Vic. Proceedings, pp. 50–51.

Carothers, W.W., Kharaka, Y.K., 1978. Aliphatic acid anions in oil-field water-implications for origin of natural gas. Am. Assoc. Pet. Geol. Bull. 62, 2441–2453.

Catling, D.C., Moore, J., 2003. The nature of coarse-grained crystalline hematite and its implications for the early environment of Mars. Icarus 165 (277–30).

Cazau, L., Uliana, M.A., 1973. El Cretácico superior continental de la Cuenca Neuquina: Buenos Aires. 5° Congreso Geológico Argentino. Proceedings 3, pp. 131–163.

Condat, P., Cruz, C., Kozlowsky, E., Manceda, R., 1990. Ambiente deposicional de las sedimentitas del Grupo Neuquén Inferior en el suroeste de Mendoza, Argentina. 11 Congreso Geológico Argentino. Proceedings 3, pp. 65–68.

Cooke, D.R., Bull, S.W., Large, R.S., McGoldrick, P.J., 2000. The importance of Oxidized brines for the formation of Australian proterozoic stratiform sediment-hosted Pb-Zn (Sedex) deposits. Econ. Geol. 95, 1–18.

Cox, D.P., Lindsey, D.A., Singer, D.A., Diggles, M.F., 2003. Sediment- Hosted Copper Deposits of the World: Deposit Models and Database: U.S. Geological Survey Open – File Report 03-107 (50p).

Cruz, C., Boll, A., Gómez Omil, R., Martínez, E., Arregui, C., Gulisano, C., Laffitte, G., Villar, H., 2002. Hábitat de hidrocarburos y sistemas de carga Los Molles y Vaca Muerta en el sector central de la Cuena Neuquina, Argentina, inProceedings of the 5° Congreso de Exploración y Desarrollo de Hidrocarburos Proceedings CD-ROM 20 p.

Darnley, A.G., 1960. Petrology of some Rhodesian Copperbelt orebodies and associated rocks. Institute of Mining and Metallurgy Transactions 69, pp. 137–173.

De Ferrariis, C., 1968. El Cretácico del norte de la Patagonia. 3° Jornadas Geológicas Argentinas. 1, pp. 121–144.

DeGolyer, E., 1924. The occurrence of vanadium and nickel in petroleum. Econ. Geol. 19, 550–558.

Dickinson, W.R., Beard, L.S., Brakenridge, G.R., Erjavec, J.L., Ferguson, R.C., Inman, K.F., Knepp, R.A., Lindberg, F.A., Ryberg, P.T., 1983. Provenance of North American Phanerozoic sandstones in relation to tectonic setting. Geol. Soc. Am. Bull. 94, 222–235. http://dx.doi.org/10.1130/0016-7606.

DiGiulio, A., Ronchi, A., Sanfilippo, A., Tiepolo, M., Pimentel, M., Ramos, V.A., 2012. Detrital zircon provenance from the Neuquén Basin (south-central Andes): cretaceous geodynamic evolution and sedimentary response in a retroarc-foreland basin. Geology 40 (6), 559–562.

Einaudi, M.T., Hedenquist, J.W., Inan, E.E., 2003. Sulfidation state of fluids in active and extinct hydrothermal systems: transitions from porphyry to epithermal environments. In: Simmons, S.F., Graham, I. (Eds.), Volcanic, geothermal and ore-forming fluids:

Rulers and witnesses of processes within the earth. Economic Geology Special Publication 10 (343 p., Boulder).

Emery, D., Myers, R.J., Young, R., 1990. Ancient subaerial exposure and freshwater leaching in sandstones. Geology 18, 1178–1181.

Fernández Aguilar, R., 1945. Los yacimientos de areniscas cupríferas del Neuquén. Dirección de Minas, Geología e Hidrología, Publicación, 58, 1-27 (Buenos Aires).

Folk, R.L., Andrews, P.B., Lewis, D.W., 1970. Detrital sedimentary rock classification and nomenclature for use in New Zealand. J. Geol. Geophys. 13, 937–968. http://dx.doi.org/10.1080/00288306.1970.10418211.

Garden, I.R., Guscott, S.C., Burley, S.D., Foxford, K.A., Walsh, J.J., Marshall, J., 2001. An exhumed palaeo-hydrocarbon migration fairway in a faulted carrier system, Entrada Sandstone of SE Utah, USA. Geofluids 1, 195–213.

Garrido, A.C., 2000. Estudio estratigráfico y reconstrucción paleoambiental de las secuencias fosilíferas continentales del Cretácico Superior en las inmediaciones de Plaza Huincul, provincia del Neuquén. Undergrauate Thesis Escuela de Geología de la Facultad de Ciencias Exactas, Físicas y Naturales. Universidad Nacional de Córdoba (78 p.).

Garrido, A.C., 2011. El Grupo Neuquén (Cretácico Tardío) en la Cuenca Neuquina. In: Leanza, H., Arregui, C., Carbone, O., Danielli, J., Vallés, J. (Eds.), Geología y Recursos Naturales de la Provincia del Neuquén, Relatorio del 18º Congreso Geológico Argentino, pp. 231–244 (Neuquén).

Giusiano, A., Franchini, M., Impiccini, A., O'Leary, S., 2006. Mineralización de Cu asociada a bitumen en las areniscas cretácicas, prospecto Barda González, Neuquén, Argentina: Antofagasta. 11 Congreso Geológico Chileno. Proceedings 2, pp. 255–258.

Giusiano, A., Bouhier, E., 2009. Mineralización de Cu en el Grupo Neuquén vinculada a la migración de hidrocarburos. Dorso de los Chihuidos, Neuquén, Argentina. Boletín de Informaciones Petroleras 11, pp. 6–18.

Giusiano, A., Franchini, M., Impiccini, A., Pons, M.J., 2008. Mineralización de Cu en sedimentitas Mesozóicas del Grupo Neuquén y hábitat de los hidrocarburos en la Dorsal de Huincul Neuquén. 17 Congreso Geológico Argentino, Simposio de Mineralogía y Metalogenia. Proceedings 2, pp. 769–770.

Goldhaber, M.B., Reynolds, R.L., Campbell, J.A., Wanty, R.B., Grauch, R.I., Northrop, R., 1990. Part II. Mechanism of ore and gangue mineral formation at the interface between brine and meteoric water. In: Northrop, H.R., Goldhaber, M.B. (Eds.), Genesis of the Tabular-Type Vanadium–Uranium Deposits of the Henry Basin. Utah. Economic Geology. 85, pp. 236–250.

Granero Hernández, A., Schmid, J., 1956. Estudio geológico económico de las areniscas cupríferas de la zona de Plaza Huincul. Dirección General de Fabricaciones Militares, Informe 191 (93 p., Buenos Aires).

Hahn, G.A., Thorson, J.P., 2006. In: Bon, R.L., Gloyn, R.W., Park, G.M. (Eds.), Geology of the Lisbon Valley sandstone-hosted disseminated copper deposits, San Juan County, Utah. Geological Association Publication, Utah, pp. 511–533.

Haynes, D.W., Bloom, M.S., 1987. Stratiform copper deposits hosted by low-energy sediments: IV. Aspects of sulfide precipitation. Econ. Geol. 82, 876–893.

Herrero Ducloux, A., 1939. Estratigrafía tectónica de los Estratos con Dinosaurios del Neuquén. 2° Reunión de Geólogos y Geofísicos de YPF. Bol. Inf. Petrol. 16 (180), 16–17.

Herrero Ducloux, A., 1946. Contribución al conocimiento geológico del Neuquén extraandino. Bol. Inf. Petrol. 23 (226), 245–281.

Hillier, S., 1993. Origin, diagenesis, and mineralogy of chlorite minerals in Devonian lacustrine mudrocks, Orcadian Basin, Scotland. Clays Clay Miner. 41, 240–259.

Hillier, S., Wilson, M.J., Merriman, R.J., 2006. Clay mineralogy of the Old Red Sandstone and Devonian sedimentary rocks of Wales, Scotland and England. Clay Miner. 41, 433–471.

Hitzman, M., Kirkham, R., Broughton, D., Thorson, J., Selly, D., 2005. The sediment-hosted stratiform copper ore system. In: Hedenquist, J.W., Thompson, J.F.H., Goldfarb, R.J., Richards, J.P. (Eds.), Economic Geology 100th Anniversary Volume, Littleton, pp. 609–642.

Hornibrook, E.R.C., Longstaffe, F.J., 1996. Berthierine from the Lower Cretaceous Clearwater Formation, Alberta, Canada. Clay Clay Miner. 44, 1–21. http://dx.doi.org/10.1346/CCMN.1996 .0440101.

James, N.P., Choquette, P.W., 1990. Limestone the meteoric diagenetic environment. In: McIlreath, I.A., Morrow, D.W. (Eds.), Diagenesis. Geoscience, Canada 11, pp. 161–164.

Ketzer, J.M., Morad, S., Amorosi, A., 2003. Predictive diagenetic clay-mineral distribution in silisiclastic rocks within sequence stratigraphic framework. In: Worden, R.H., Morad, S. (Eds.), Clay Mineral Cements in Sandstones, 34 Special Publication of International Association of Sedimentologists. Blackwell Publishing Ltd., Oxford (43–61p.).

Klappa, C.F., 1978. Biolithogenesis of Microcodium: elucidation. Sedimentology 25, 489–522. http://dx.doi.org/10.1111/sed.1978.25.issue-4.

Kosir, A., 2004. Microcodium revisited: root calcification products of terrestrial plants on carbonate rich substrates. J. Sediment. Res. 74, 845–857. http://dx.doi.org/10.1306/040404740845.

Kraus, M., Wells, T., 1999. Recognizing avulsion deposits in the ancient stratigraphical record. In: Smith, N., Rogers, J. (Eds.), Fluvial Sedimentology, 6º International Association of Sedimentologists Special Publication Oxford 28, pp. 251–268.

Langmuir, D., 1978. Uranium solution-mineral equilibria at low temperatures with applications to sedimentary ore deposits. Geochim. Cosmochim. Acta 42, 547–556.

Leanza, H., Hugo, C., 1997. Hoja Geológica 3969—II Picún Leufú, Provincias del Neuquén y Río Negro: Instituto de Geología y Recursos Naturales, SEGEMAR, Boletín. Buenos Aires. p. 218 (135).

Leanza, H.A., Hugo, C.A., Repol, D., González, R., Danieli, J.C., 2005. Hoja Geológica 3969-I, Zapala. Provincia del Neuquén. Instituto de Geología y Recursos Minerales, Servicio Geológico Minero Argentino. Boletín 275 (128 p., Buenos Aires).

Leanza, H.A., Mazzini, A., Corfu, F., Llambías, E.J., Svensen, H., Planke, S., Galland, O., 2013. The Chachil Limestone (Pliensbachiane earliest Toarcian) Neuquén Basin, Argentina: U-Pb age calibration and its significance on the Early Jurassic evolution of southwestern Gondwana. J. S. Am. Earth Sci. 42, 171–185.

Legarreta, L., Gulisano, C.A., 1989. Análisis estratigráfico secuencial de la Cuenca Neuquina (Triásico Superior-Terciario Inferior). In: Chebli, G., Spaletti, L. (Eds.), Cuencas Sedimentarias Argentinas. In 10º Congreso Geológico Argentino San Miguel de Tucumán. Serie Correlación Geológica 6, pp. 221–243.

Legarreta, L., Cruz, C.E., Laffitte, G.A., Villar, H.J., 2003. Source rocks, reserves and resources in the Neuquén Basin, Argentina: Mass-balance approach and exploratory potential, International Congress and Exhibition of the American Association of Petroleum Geologists, abs., Barcelona, 87, 13(Supplement).

Lyons, W.A., 1999. Las areniscas cupríferas del Neuquén. In: Zapettini, E.O. (Ed.), Recursos Minerales de la República Argentina. Instituto de Geología y Recursos Minerales, SEGEMAR. Anales 35, pp. 1149–1158.

MacGowan, D., Surdam, R.C., 1988. Difunctional carboxylic acid anions in oil-field waters. Org. Geochem. 12, 245–259.

Madejová, J., Balan, E., Petit, S., 2011. Application of vibrational spectroscopy to the characterization of phyllosilicates and other industrial minerals. EMU Notes Mineral. 9 (6), 171–226.

Malone, P., Saavedra, C., Vergani, G., Ferrero, J.C., Limeres, M. y Schiuma, M. 2002. Los Reservorios del Grupo Cuyo Superior. Rocas Reservorios de la Cuencas Productivas de Argentina. In 5º Congreso de Exploración y Desarrollo de Hidrocarburos, Proceedings, 277-302.

Maretto, H., Pángaro, F., 2005. Edad de formación de algunas de las grandes estructuras del engolfamiento de la Cuenca Neuquina: Actividad tectónica durante la depositación de la Fm. Quintuco. In 6° Congreso de exploración y Desarrollo de Hidrocarburos Proceedings,CDROOM11p.

Miall, A., 1996. The Geology of Fluvial Deposits. Springer, New York (582 pp.).

Montagna, A., Zardo, E.B., Celentano, M.A., 2010. Caracterización petrofísica a partir de la integración de registros eléctricos y datos de roca de la Fm. Mulichinco del yacimiento Rincón del Mangrullo, Neuquén, Argentina. Petrotecnia 6, 82–96.

Moore, D.M., Reynolds Jr., R., 1997. X-ray diffraction and the identification and analysis of clay minerals. Oxford University Press, New York (378 pp.).

Morrison, S.J., Parry, W.T., 1986. Dioctahedral corrensite from Permian red beds, Libson Valley, Utah. Clay Clay Miner. 34, 613–624.

Mosquera, A., Ramos, V.A., 2006. Intraplate deformation in the Neuquén Embayment. In: Kay, S.M., Ramos, V.A. (Eds.), Evolution of an Andean Margin: A Tectonic and Magmatic View from the Andes to the Neuquén Basin (35°–39°S Lat). Geological Society of America Special Paper, Boulder 407, pp. 97–123.

Mosser-Ruck, R., Cathelineau, M., Guillaume, D., Charpentier, D., Rousset, D., Barres, O., Michau, N., 2010. Effects of temperature, pH and iron/clay and liquid/clay ratios on experimental conversion of dioctahedralsemectite to berthierine, chlorite, verminculite or saponite. Clay Clay Miner. 58 (2), 280–291.

Murakami, T., Sato, T., Inoue, A., 1999. HRTEM evidence for the process and mechanism of saponite-to-chlorite conversion through corrensite. Am. Mineral. 84, 1080–1087.

Newman, A., Brown, G., 1987. The chemical constitution of clays. In: Newman, A. (Ed.)-Chemistry of Clays and Clay Minerals: Mineralogical Society Monograph 6, pp. 1–129.

Parnell, J., Carey, P.F., 1995. Emplacement of bitumen (asphaltite) veins in the Neuquén Basin, Argentina. Am. Assoc. Pet. Geol. Bull. 79, 1798–1816.

Parras, A., Casadío, S., Náñez, C., Concheyro, A., Griffin, M., 2004. The Cretaceous/Paleogene boundry in the Neuquén Basin, northern Patagonia, Argentina. In 10° Reunión Argentina de Sedimentología, Siponsio K/T, Proceedings, p. 195.

Paz, M., 2015. Relación entre la mineralización de Cu y bitumen en el prospecto La Cuprosa Dorsal de Huincul, Neuquén. Geology degree thesis Universidad Nacional de Río Negro, 50 p, Gral. Roca.

Paz, M., Pons, M.J., Giusiano, A., Franchini, M., 2014. Facies diagenéticas y su vinculación con la circulación de hidrocarburos en la Formación Portezuelo, Dorsal de Huincul Neuquén. 9° Congreso de Exploración y Desarrollo de Hidrocarburos, Proceedings, pp. 63–70.

Pons, M.J., Franchini, M.B., Giusiano, A., Impiccini, A., Godeas, M., 2009. Alteraciones, mineralización de Cu y Bitumen en areniscas Cretácicas del Prospecto Barda González, Neuquén, Argentina. Rev. Geol. Argent. 64 (3), 321–333.

Pons, M.J., Franchini, M., Giusiano, A., Maydagán, L., Rainoldi, A.L., 2014. Mineralización de Cu (V-U) en la Formación Huincul, prospecto Tordillos, Cuenca Neuquina. Rev. Asoc. Geol. Argent. 71, 537–552.

Pons, M.J., Franchini, M., Meinert, L., Giusiano, A., Impiccini, A., Beaufort, D., Patrier, P., Rainoldi, A.L., 2015a. Characterization of the diagenesis, alteration and Cu-mineralization in the Cretaceous sedimentary rocks of the Tordillos deposit, Neuquén Basin, Argentina. SEG CODES-Conference, Tasmania, Proceedings, (1 p.).

Pons, M.J., Rainoldi, A, Franchini, M.B., Beaufort, D., Impiccini, A., Cessartti, N., Giusiano, A., Patrier, P., 2015b. Mineralogical signature of hydrocarbon circulation in Cretaceous red beds of the Barda González area, Neuquén Basin. Am. Assoc. Pet. Geol. Bull. 99 (3), 525–554.

Rainoldi, A.L., 2015. Alteración regional de las sedimentitas Cretácicas en la Dorsal de Huincul y en el Dorso de Los Chihuidos, su relación con la mineralización de Cu y con los hidrocarburos Neuquén (PhD thesis in Geology) Universidad Nacional del Sur, p. 251 (Bahía Blanca).

Rainoldi, A.L., Franchini, M., Beaufort, D., Impiccini, A., Giusiano, A., Patrier, P., Pons, J., 2014. Bleaching of red beds at large scale related to hydrocarbons up flow. Los Chihuidos High (37°50′S, 69°27′W), Neuquén Basin, Argentina. J. Sediment. Res. 84, 373–393.

Rainoldi, A.L., Franchini, M., Beaufort, D., Mozley, P., Giusiano, A., Cesaretti, N., Patrier, P., Pons, M.J., 2015. Mineral reaction associated with hydrocarbons paleomigrations in the Huincul High, Neuquén Basin, Argentina. Geol. Soc. Am. Bull. 127, 1711–1729. http://dx.doi.org/10.1130/B31201.1.

Ramos, V.A., 1975. Los ciclos sedimentarios y biorhexistacia en el control de las manifestaciones cupríferas del Neuquén extraandino, Argentina. Congreso Ibero-Americano de Geología Económica, Proceedings 5, pp. 373–394.

Ramos, V.A., 1981. Descripción Geológica de la Hoja 33c, Los Chihuidos Norte. Provincia del Neuquén: Servicio Geológico Nacional, Buenos Aires, Boletín 182, pp. 1–103.

Robinson, D., Santana de Zamora, A., 1999. The smectite to chlorite transition in Chipilapa geothermal system, El Salvador. Am. Mineral. 84, 607–619.

Rodríguez, M.F., 2011. El Grupo Malargüe (Cretácico Tardío-Paleógeno temprano) en la Cuenca Neuquina. In: Leanza, H., Arregui, C., Carbone, O., Danielli, J., Vallés, J. (Eds.), Geología y Recursos Naturales de la Provincia del Neuquén, Relatorio del 18° Congreso Geológico Argentino, pp. 245–264 (Neuquén).

Roduit, N., 2008. JMicroVision: Image Analysis Toolbox for Measuring and Quantifying Components of High-Definition Images. Version 1.2.7: http://www.jmicrovision. com, (accessed 26 March 2015).

Rose, A.W., 1976. The effect of aqueous chloride complexes in the origin of red-bed copper and related deposits. Econ. Geol. 71, 1036–1048.

Russell, J.D., Fraser, A.R., 1994. Infrared methods: Clay Mineralogy: Spectroscopic and Determinative Methods Edited by Wilson Chapman and Hall. pp. 11–67 (London).

Sánchez, M.L., Rossi, S.M., Armas, P., 2008. Análisis estratigráfico secuencial de las Formaciones Huincul y Lisandro del Subgrupo Río Limay (Grupo Neuquén-Cretácico Tardío) en el departamento El Cuy, Río Negro, Argentina. Lat. Am. J. Sedimentol. Basin Anal. 15, 1–26.

Schiuma, M., Saavedra, C., Malone, P., Cevallos, M., Rebori, L., Vergani, G., 2002. Los reservorios del Gupo Lotena, Argentina. In:, Rocas Reservorios de las Cuencas Productivas de la Argentina. 5° Congreso de Exploración y Desarrollo de Hidrocarburos Proceedings, pp. 303–334.

Schmidt, N.G., Alonso, M., 2015. Informe anual 2014 de la producción no convencional de petróleo y gas en la Provincia de Neuquén. Petrotecnia 56 (3), 48–60.

Sillitoe, R.H., 2005. Supergene oxidized and enriched porphyry copper and related deposits: Economic Geology 100th Anniversary volume. pp. 723–768.

Silvestro, J., Zubiri, M., 2008. Convergencia oblicua:Modelo estructural alternativo para la Dorsalneuquina (39° S)-Neuquén. Rev. Asoc. Geol. Argent. 63 (1), 49–64.

Sosic, M., 1978. Recursos hídricos subterráneos. In: Rolleri, E.O. (Ed.), Geología y Recursos Naturales del Neuquén. Relatorio 7° Congreso Geológico Argentino, Buenos Aires, pp. 309–323.

Sugimoto, T., Waki, S., Itoh, H., Muramatsu, A., 1996. Preparation of monodisperse platelet-type hematite particles from a highly condensed β-FeOOH suspension. Coll. Surf. A 109, 155–165.

Surdam, R.C., Crossey, L.J., Hagen, E.S., Heasler, H.P., 1989. Organic-inorganic interactions and sandstone diagenesis. Am. Assoc. Pet. Geol. Bull. 73, 1–32.

Sverjensky, D., 1987. The role of migrating oil field brines in the formation of sediment-hosted Cu rich deposits. Econ. Geol. 82, 1130–1141.

Uliana, M.A., Biddle, K.T., Cerdán, J., 1989. Mesozoic extension and the formation of Argentine sedimentary basins. In: Tankard, A.J., Balkwill, H.R. (Eds.), Extensional tectonics

and stratigraphy of the North Atlantic margins: American Association of Petroleum Geologists Memoir 46, pp. 599–614.

Velde, B., 1985. Clay Minerals: A Physico-Chemical Explanation of their Occurrence: Developments in Sedimentology 40: pp. 427 Amsterdam. Elsevier, Netherlands.

Vergani, G.D., Tankard, A.J., Belotti, H.J., Welsink, H.J., 1995. Tectonic evolution and paleogeography of the Neuquén Basin, Argentina. In: Tankard, A.J., Suárez, S.R., Welsink, H.J. (Eds.), Petroleum Basins of South America: American Association of Petroleum Geologists Memoir 62. Tulsa, EEUU, pp. 383–402.

Vottero, J., González, J.M., 2002. Los reservorios de la Formación Mulichinco. Rocas Reservorios de la Cuencas Productivas de Argentina. 5° Congreso de Exploración y Desarrollo de Hidrocarburos, Proceedings, pp. 383–400.

Walker, T.R., 1976. Red beds in the western interior of the United States: U.S. Geol. Surv. Prof. Pap. 853, 49–56.

Walker, T.R., 1989. Application of diagenetic alterations in redbeds to the origin of copper in stratiform copper deposits. In: Boyle, R.W., Brown, A.C., Jefferson, C.V., Jowett, E.C., Kirkham, R.V. (Eds.), Sediment-hosted stratiform copper deposits: Geological Association of Canada. Special Paper 36, pp. 85–96.

Wichmann, L.A., 1972. Los estratos con dinosaurios y su techo en el este del territorio de Neuquén. Dirección General de Minería, Geología e Hidrología, Publicación 32, pp. 3–25 (Buenos Aires).

Willey, L.M., Kharaka, Y.K., Presser, T.S., Rapp, J.B., Barnes, I., 1975. Short chain aliphatic acid anions in oil fieldwaters and their contribution to the measured alkalinity. Geochim. Cosmochim. Acta 39, 1707–1711. http://dx.doi.org/10.1016/0016-7037(75)90092-7.

Worden, R.H., Morad, S., 2003. Clay minerals in sandstones: controls on formation, distribution and evolution. In: Worden, R.H., Morad, S. (Eds.), Clay Mineral Cements. In Sandstones. 34 Special Publication of International Association of Sedimentologists. Blackwell Publishing Ltd., Oxford, pp. 1–41.

Zavala, C., Martínez Lampe, J.M., Fernández, M., Di Meglio, M., Arcuri, M., 2008. El diacronismo entre las Formaciones Tordillo y Quebrada del Sapo (Kimeridgiano) en el sector sur de la cuenca neuquina. Rev. Asoc. Geol. Argent. 63, 754–765.

Zientek, M.L., Hayes, T.S., Niki, E., Wintzer, N.E., Heather, L.P., 2015. Qualitative Assessment of Sediment-Hosted Stratabound Copper Permissive Tracts. In: Zientek, M.L., Hammarstrom, J.M., Johnson, K.M. (Eds.), Qualitative Assessment of Selected Areas of the World for Undiscovered Sediment Hosted Stratabound Copper Deposits 3-23 (143 pp.).